arXiv:1008.5317v1 [physics.atom-ph] 30 Aug 2010

Anna Simon

Correlated radiative electron capture in ion-atom collisions

Ph.D. Dissertation

prepared under the supervision of

Prof. Andrzej Warczak



Marian Smoluchowski Institute of Physics

Jagiellonian University

Kraków, April 2010

Abstract

Radiative double electron capture (RDEC) is a one-step process where two free (or quasi-free) target electrons are captured into a bound state of the projectile, e.g. into an empty K-shell, and the energy excess is released as a single photon. This process can be treated as a time inverse of double photoionization. However, unlike in case of photoionization experiments, bare ions are used during RDEC observations. Thus, RDEC can be considered as the simplest, clean tool for investigation of the electron-electron interaction in the presence of electromagnetic fields generated during ion-atom collisions.

Within this dissertation, the 38 MeV O^{8+} + C experiment, conducted at Western Michigan University using the tandem Van de Graaff accelerator, is discussed and the first experimental evidence of the RDEC process is presented. The cross section obtained experimentally is compared to the latest theoretical calculations.

Abstrakt

Skorelowany radiacyjny wychwyt dwóch elektronów (RDEC) jest procesem, podczas którego dwa swobodne (albo kwaziswobodne) elektrony tarczy wychwytywane są do stanu związanego pocisku (np. nieobsadzonej powłoki K), a różnica energii pomiędzy końcowym a początkowym stanem eletronów emitowana jest w postaci pojedynczego fotonu. Proces ten można traktować jako odwrócenie w czasie podwójnej fotojonizacji. Jednakże, w przeciwieństwie do eksperymentów dedykowanych fotojonizacji, do obserwacji RDEC stosuje się jony całkowicie pozbawione elektronów, co pozwala na wyeliminowanie tła pochodzącego od elektronów nie biorących bezpośrednio udziału w badanym procesie. RDEC może być więc traktowany jako najprostsze narzędzie do badania oddziaływania elektron-elektron w obecności pola elektromagnetycznego generowanego podczas zderzenia.

Rozprawa ta poświęcona jest procesom atomowym zachodzącym w zderzeniach O^{8+} + C przy energii 38 MeV podczas eksperymentu przeprowadzonego przy użyciu alceleratora Van de Graaffa w Western Michigan University. Przedstawione zostało w niej pierwsze doświadczalne potwierdzenie procesu RDEC. Uzyskany eksperymentalnie przekrój czynny został porównany z wynikami najnowszych przewidywań teoretycznych.

Acknowledgements

First, I would like to give my sincere thanks to my supervisor, Professor Andrzej Warczak. He offered me advice, patiently supervised me and always guided me to the correct direction. I have learned much from him, without his help I would have never finished my dissertation successfully.

Special thanks are also given to Professor John A. Tanis. He is the one who invited me to Western Michigan University for my research during the 2008-2009 academic year. His help and encouragement made me feel confident enough to fulfill my desires and to overcome the difficulties I encountered. His understanding, encouragement and personal guidance have provided a good basis for my thesis. It is not sufficient to express my gratitude with such a few words.

I am very grateful to Professor Bogusław Kamys, the Head of the Nuclear Physics Division at the Institute of Physics, Jagiellonian University and Professor Paul Pancella, the Chair of Physics Department, Western Michigan University, for the financial support of my stay at WMU.

Additionally, I owe my most sincere gratitude to Dr. Asghar Kayani for his patience while teaching me how to operate the WMU tandem Van de Graaff accelerator and his willingness to immediately solve any beam related problems during my experiment. My sincere thanks should also go to Rick Welch and Allan Kern for their help with the maintenance of the experimental setup.

I would also like to thank Janusz Kopczyński, Adam Malarz and Adam Mucha for their care and support during my work at Jagiellonian University.

I am also very grateful to Prof. Thomas Stöhlker, the Head of Atomic Physics Group at GSI, Darmstadt, who frequently invited me to join his group's experiments during which I had a chance to learn the secrets of the experimental work of atomic physicists. I'm grateful to Dr. Angela Bräuning-Demian and Dr. Christophor Kozhuharov for inspiring conversations that led to many ideas implemented in this thesis.

I am very grateful to my friends, David Cassidy, Buddhika Dassanayake, Małgorzata Makuch, Dagmara Rozpędzik and Andrzej Pezarski, for always being there for me.

Last, but not least, I wanted to thank my parents for their support and encouragement.

Table of Contents

List of Tables **vii**

List of Figures **ix**

List of Symbols and Abbreviations **1**

1 Introduction **2**

2 Atomic processes during ion-atom collisions at low energy **5**

2.1 Nonradiative electron capture (NREC) 5

2.2 Radiative electron capture (REC) 6

2.3 Bremsstrahlung 8

2.3.1 Electron bremsstrahlung 10

2.3.2 Nucleus-nucleus bremsstrahlung (NB) 13

2.4 Multielectron capture processes, noncorrelated double radiative electron capture (DREC) 14

2.5 Projectile ionization – electron loss 17

3 Radiative double electron capture (RDEC) **18**

3.1 Initial experiments dedicated to RDEC 18

3.2 Recent theoretical approach to RDEC 21

4 Experimental setup at Western Michigan University **27**

4.1 Van de Graaff accelerator 27

4.2 Beam line setup at Western Michigan University 29

4.3 Data acquisition system 33

5 Data analysis **36**

5.1 PIXE analysis of the target material 37

5.2 Projectile K- and L-shell electron loss 38

5.3 Background processes 39

5.4 Pile-up of single REC photons and its contribution to the RDEC energy range of the spectrum 41

5.5 Single spectra analysis 44

5.6 Coincidence spectra analysis 45

6 The RDEC cross section **55**

6.1 Experimental value of the RDEC cross section 55

6.2 Estimation of the $\sigma_{RDEC}/\sigma_{REC}$ ratio in the nonrelativistic approach 57

6.3 RDEC cross section based on the Yakhontov approach 57

7 Monte Carlo simulations of the x-ray spectra **59**

8 Conclusions **64**

A Statistical analysis of the observed signal **66**

List of References **69**

List of Tables

3.1 Comparison of experimentally obtained RDEC cross sections [War 95, Bed 03] and the calculated values given in [Yak 97] and [Mik 04a]. 24

3.2 The REC ($\sigma^{(1)}$), RDEC ($\sigma^{(2,\gamma)}$) and DREC ($\sigma^{(2,2\gamma)}$) cross sections and their ratios as given in [Dru 07]. 25

5.1 Results of a χ^2 test of the RDEC range of the proton induced spectrum. . . . 38

5.2 Electron loss cross sections for oxygen ions at 38 MeV estimated from the data presented in [Bom 89, Tan 91, Hip 87]. 39

5.3 Total cross sections for the background processes that were taken into account during data analysis. 41

5.4 Probabilities and count rates of the processes that might contribute to the x-ray spectrum in the RDEC range. For more information see text. 42

5.5 Calculated positions of the RDEC and REC peaks in the x-ray spectrum corresponding to different combinations of the initial and final states of the captured electrons. All values are given in keV. 44

5.6 Results of a χ^2 test of the RDEC range of the coincidence spectra. 45

5.7 Areas (A) of the shapes of the RDEC contributions fitted to the sum of $q-1$ and $q-2$ spectra. The FWHM of all lines was set to 0.3 keV which is the width of the carbon Compton profile. 47

6.1 Comparison of the experimental values of the RDEC cross section and the $R = \sigma^{1s^2}_{RDEC}/\sigma_{REC}$ ratio with the ones obtained from various theoretical approaches . 58

7.1 Ratios of the numbers of counts in the RDEC and REC regions obtained during Monte Carlo simulations compared with the experimental value. 63

8.1 Summary of the results of the theoretical calculations and the experiments dedicated to the RDEC process. 65

A.1 Quantiles of the χ^2 distribution for $DoF = 1$ [Kam]. 68

List of Figures

2.1 Radiative electron capture (REC). A target electron is captured into the projectile bound state and the energy excess is emitted as a single photon. 7
2.2 Example of the x-ray spectrum registered in coincidence with single electron capture during U^{92+} + N_2 collisions at 309.7 MeV/u [Swi 00]. 8
2.3 Compton profile of electrons in carbon atom. It can be noticed that the structure of the $1s$ line is much broader than that for $n = 2$ states [Big 75]. 9
2.4 Example of the bremsstrahlung process for an electron in the electromagnetic field of an ion. 9
2.5 Radiative electron capture to continuum (RECC). Target electron is captured into a continuum state of the projectile and a photon is emitted. 10
2.6 Spectra observed during the experiment of [Bed 98] for: (a) Be-target, (b) C-target. For each energy-target combination two spectra are displayedwith the upper spectrum showing the raw data and the lower spectrum with the results after background subtraction. For presentation purposes spectra were multiplied by factors; (a) Be-target: 1/20 for 75 MeV/u, 10 for 290 MeV/u; (b) C-target: 1/8 for 75 MeV/u, 10 for 150 MeV/u, 50 for 290 MeV/u. Dashed line: SEB contribution, solid line: RECC (relativistic approximation) + K-REC + SEB. Arrows show the RECC-edge energy T_r transformed to the laboratory frame. Inset in (a) represents the experimental setup. 12
2.7 Example of the contribution of various bremsstrahlung processes to the continuous x-ray spectrum during pl + Al collisions at 1 and 4 MeV [Ish 06]. It can be noticed that SEB becomes a dominating process at higher beam energy. . 13
2.8 Bremsstrahlung processes observed during p + C collisions at 2 MeV. Plot based on Fig. 3 in [Ish 06]. 14
2.9 Comparison of the DREC and RDEC processes. 15

2.10 Single electron loss cross section as given in [Hip 87]. Solid line: PWBA calculations for He^{2+} impact, dot-dashed line: includes contribution from free electron impact in CBE approximation. Symbols: $\triangle$ – Si^{8+}, $\square$ – O^{6+}, $\triangledown$ – Si^{13+}, $\circ$ and $\times$ – O^{7+}. 16

3.1 Typical x-ray spectrum obtained during argon experiment [War 95]. 19
3.2 Typical experimental x-ray spectrum obtained for uranium ions [Bed 03]. The Gaussian solid line shows the expected RDEC peak, which should be observed according to Yakhontov et al. [Yak 96, Yak 97]. 20
3.3 Universal function Q calculated as a function of the dimensionless variable ξ [Mik 04a]. 22
3.4 Universal quantity Q/H calculated as a function of the dimensionless variable ξ [Mik 04a]. 23
3.5 The ratio of the RDEC cross sections to the excited ($\sigma^{(2)}_{2^1S}$) and ground ($\sigma^{(2)}_{1^1S}$) projectile states as a function of adiabacity parameter ξ [Nef 05]. 24

4.1 Schematic view of a classical Van de Graaff accelerator: (1) lower roller, (2) upper roller, (3) charging electrode, (4) electrode collecting positive charge, (5) voltage generator, (6) spherical electrode (high voltage terminal), (7) ion source, (8) extracted ion beam. 28
4.2 Schematic view of a tandem Van de Graaff accelerator: A negative ion entering the accelerator (A^-) is accelerated by the high terminal voltage. Some of its electrons are removed while the ion passes through the stripping foil. The positive ion (A^{+q}) is repelled by the high voltage terminal, thus causing additional acceleration. 29
4.3 Schematic view of the WMU van de Graaff accelerator facility [Kay]. 30
4.4 The experimental target chamber in 1:1 scale. 31
4.5 Detection efficiency of ORTEC Si(Li) detectors [ORTa]. 32
4.6 Experimental setup. 32
4.7 Example of a time spectrum registered during the experiment. The arrow indicates the width of a time window for true coincidences (calibration 2 ns/channel). 34
4.8 Scheme of the data acquisition system. 35

5.1 Experimental single x-ray spectra. In all spectra: solid line – 38 MeV O^{8+} + C. (a) dashed line – O^{8+} data taken without the carbon foil, (b) O^{8+} data after subtraction of the Al K-α line, (c) dotted line – 38 MeV O^{7+} + C, (d) dot-dashed line – 2.375 MeV protons on carbon. 48

5.2 X rays registered for O^{8+} + C collisions in coincidence with ions which captured (a) two electrons and (b) one electron. Solid line is the sum of the REC Compton profile and the Gaussian shape of the oxygen K-α line fitted to the spectrum. 49

5.3 Proton induced x-ray spectrum. Solid line: the RDEC range; dashed line: region considered during background estimation. 50

5.4 Background structure in the single x-ray spectrum. The bremsstrahlung contribution includes all the relevant processes (SEB + AB + NB) discussed in the text. The spectrum is completely dominated by the REC structure. . . . 50

5.5 N_{RDEC}/N_{REC} ratio in the $q-1$ coincidence spectra as a function of beam intensity. 51

5.6 O^{8+} spectrum taken without the carbon foil (red line) normalized to the data taken with the foil (black line). 51

5.7 Double structure of the REC line resolved after subtraction of the Al K-α line. 52

5.8 Possible RDEC transitions (a) and the structure of the produced x-ray spectrum (b) when equal cross sections for all the partial processes are assumed. Black line – the sum of all contributions. Additionally, corresponding RDEC spectra obtained experimentally in single (c) and double (d) charge exchange channels are presented. 53

5.9 The sum of spectra registered in single and double charge exchange channels with a fit of all possible combinations of the RDEC transitions. Fitting parameters are given in Table 5.7. 54

7.1 Geometry of the experimental setup implemented in the Monte Carlo simulation, b_w – the beam diameter, d_t – target thickness in mm. The x-axis is perpendicular to the picture plane. 60

7.2 Monte Carlo simulated x-ray spectra: (a) no RDEC included, (b) the RDEC cross section as given by Nefiodov, (c) $\sigma^{1s^2}_{RDEC} = 3$ b and $\sigma^{1s^1 2s^1}_{RDEC} = 2.1$ b – cross sections values for which MC simulation gives the results closest to the experimental data. (d) Experimentally obtained singles spectrum. 61

7.3 The RDEC range of the x-ray spectra. Results of simulations: (a) no RDEC included, (b) the RDEC cross section as given by Nefiodov, (c) $\sigma^{1s^2}_{RDEC} = 3$ b and $\sigma^{1s^1 2s^1}_{RDEC} = 2.1$ b – cross sections values for which MC simulation gives the results closest to the experimental data. (d) Experimentally obtained single spectrum 62

A.1 Example of an experimentally obtained spectrum with a structure within the AB range. 67

Chapter 1

Introduction

Since the first observation of the photoelectric effect by Hertz [Her 87] and its explanation by Einstein [Ein 05] the interaction between electrons and light has been of considerable attention. The fundamental process occurring due to this interaction is photoionization, where absorption of a photon of energy $\hbar\omega$ results in the emission of an electron:

$$A + \hbar\omega \rightarrow A^{+} + e^{-}. \tag{1.1}$$

Simple photoionization experiments usually are restricted to neutral atoms, where the influence of the electrons, which do not participate in the process directly, cannot be neglected. This complicates comparison of the experimental results with theoretical predictions.

However, based on the principle of detailed balance [Lan 79, Bey 03] the photoionization can be studied via the time reversed processes, i.e. radiative recombination (RR) and radiative electron capture (REC) [Ich 94, Ich 96, Eic 95a]. During these processes a free (RR) or loosely bound (REC) electron is captured to the bound state of the projectile and a photon with energy equal to the difference between the final and initial electron states is emitted. Unlike single photoionization of multielectron systems, REC has been investigated for bare ion-atom interactions [Sto 92, Sto 94] and offers clean conditions for exploration of photoionization with only one electron, allowing for observation of pure photon-electron interactions.

During the last thirty years double photoionization has been of considerable interest [Dal 94, and references therein]. As a photon typically interacts only with one electron, double photoionization is caused by the electron-electron interaction [Smi 89]. However, double photoionization studies have been performed mainly for low Z atoms, such as He [Ber 93, Tiw 82, Car 81], Ne [Sai 92, Sch 93, Car 77], and Ar [Lab 87, Car 77]. This is due to the background contributions from other electrons for high Z systems, which make the subtle

electron correlation effects difficult to observe. Fortunately, similar to single photoionization, double photoionization can be studied by means of the time inversed process – RDEC, for which this background is absent. Radiative double electron capture (RDEC) involves transfer of two target electrons into a bound state of the projectile with simultaneous emission of a single photon [War 95, Bed 03]. Since bare ions are used during the experiment, RDEC can be considered as the simplest, clean tool for investigation of the electron-electron interaction [War 95] in the presence of electromagnetic fields generated during ion-atom collision. Thus, investigation of the RDEC process can provide crucial information necessary for a proper description of electron correlations within atomic systems and provide data required to define the wave function of two correlated electrons in the projectile continuum.

During the last twenty years the RDEC process was addressed not only experimentally [War 95, Bed 03], but also theoretically [Mir 89, Yak 96, Yak 97]. The calculations were found to be in disagreement with the experimental data [Bed 03] and verification of the RDEC process was not possible. The more recent calculations not only explained previous experimental results, but also suggested the choice of low energy mid-Z ($Z \leq 35$) collision systems for observation of RDEC [Mik 04a, Mik 04b, Dru 07]. It is also noted that for these systems capture to an excited $1s^1 2s^1$ state might significantly enhance the process and contribute to the observed x-ray spectra [Nef 05]. These calculations provided the main motivation for yet another experiment dedicated to the RDEC process. To fully take advantage of the new calculations, two collision systems at two different accelerator complexes were chosen:

- Xe^{54+} + C at 20 MeV/u, to be performed at GSI, Darmstadt in Germany,
- O^{8+} + C at 2.375 MeV/u, realized by means of the Van de Graaff accelerator at WMU, Kalamazoo, MI, USA.

So far the WMU experiment was carried out. During six months of the experiment preparations and data taking, 43 days of beam time were used. At the moment when this thesis is being written the GSI beam time is still pending.

Within this dissertation the O^{8+} + C at 38 MeV experiment is discussed and the first experimental evidence of the RDEC process is presented. The cross section obtained experimentally is compared with the latest theoretical calculations [Mik 04a, Mik 04b, Nef 05, Dru 07].

This thesis begins with an introduction to the most important atomic processes that occur during ion-atom collisions. In Chapter 2 special attention is paid to the processes which

add to the background for the x-ray spectrum registered during the experiment and formulae allowing for estimations of contributions of these processes are suggested. Chapter 3 addresses the RDEC process in detail. The history of the experimental approach and the theoretical calculations of the RDEC cross section are presented. Additionally, this chapter focuses on the recent theoretical calculations which were the main motivation for the experiment discussed in this dissertation. The goal of the experiment was the observation of x rays emitted during collisions of bare oxygen ions with carbon atoms. The x-ray spectra were registered in coincidence with ongoing particles which underwent single or double charge exchange. The experimental setup which allowed for achieving this goal is presented in Chapter 4. The operation principle of a Van de Graaff accelerator is explained and the construction of the target chamber, particle spectrometer and x-ray detector are described in detail. Chapter 5 is dedicated to data analysis, with a particular focus on processes that may contribute to the x-ray spectrum within the RDEC region. Various approaches to estimation of the background and calculations of the cross section are discussed. In Chapter 6 the experimentally obtained RDEC cross section is compared with the theoretical value and the possible reasons for the obtained discrepancy are given. In Chapter 7 results of the Monte Carlo simulations of the x-ray spectrum generated during the O^{8+} + C collisions are compared with the experimental results. Finally, in Chapter 8 suggestions for further investigations of the RDEC process are given, with indication of necessary improvements of the experimental setup.

Chapter 2

Atomic processes during ion-atom collisions at low energy

Interaction between an incoming ion and a target atom may lead to many different atomic processes, such as:

- ionization, mainly of the target atom, as the electrons are usually less bound to a light target than to a partially ionized projectile,
- electron transfer from the target to the projectile,
- excitation of both target and projectile states – such states deexcite after the collision emitting characteristic x rays.

Within the following sections the most important processes that were considered competitive to RDEC for the presented experiment are discussed.

2.1 Nonradiative electron capture (NREC)

The Coulomb interaction between the projectile and the target electrons can lead to a process called Coulomb capture or nonradiative electron capture (NREC). Here, the energy difference between the initial and final state of the electron is converted into the kinetic energy of the collision partners. The most convenient and frequently used scaling formula that estimates the cross section for nonradiative electron capture is the one given by Schlachter [Sch 83]. It is a semiempirical formula which allows for calculation of the σ_{NREC} as a function of the projectile energy for various projectiles with an accuracy better than 30%.

The NREC process occurs mainly at the velocity matching condition $v \approx v_e$, where v_e is the velocity of the captured electron, bound in the target atom. For $v \gg v_e$ in the nonrelativistic approximation, as shown for example in [Eic 07], the NREC cross section scales as:

$$\sigma_{NREC} \sim \frac{Z_t^5 Z^5}{v^{12}}. \tag{2.1}$$

2.2 Radiative electron capture (REC)

Radiative electron capture (REC) is one of the best known atomic processes observed in heavy ion-atom collisions. It was first observed in early seventies of the last century [Sch 72, Kie 73, Sch 74] and since that time has been intensively studied both experimentally [Kan 95, Mok 95, Spi 79, Sto 95b, Sto 92, Sto 94, Sto 95a, Sto 97b, Sto 97a, Sto 98, Tan 81, Tan 87] and theoretically [Eic 95a, Eic 95b, Hin 87, Ich 94, Ich 96, Soh 76]. During this process capture of a single target electron is followed by a photon emission (Fig. 2.1). The energy E_{REC} of the emitted photon fulfills the energy conservation rule for this process. Thus, it is given by:

$$E_{REC} = T_r + E_B - E_{Bt} + \overrightarrow{v}\,\overrightarrow{p}, \tag{2.2}$$

where E_B and E_{Bt} are the binding energies of the projectile and target, respectively, $\overrightarrow{v}$ is the projectile velocity and $\overrightarrow{p}$ the momentum of the electron in the bound state of the target. $T_r = (m_e/m_p)E$ is the kinetic energy of the quasifree target electron calculated in the projectile's frame of reference.

The REC line observed during experiments is much broader than the characteristic x-ray lines, as can be observed in Fig. 2.2, which is due to the velocity distribution of target electrons. This distribution is described by Compton profile $\Im(p_z)$ [Big 75], which gives the probability of finding an electron with a given momentum projection p_z, where (for ion-atom collisions) the z-axis is defined by the projectile velocity. The Compton profile depends on the target atomic number Z_t and its width increases with increasing Z_t. Moreover, the width depends on the binding energy and is smaller for loosely bound electrons, than for a tightly bound $1s$ electron as shown in Fig. 2.3.

When the binding energy of the target electron is much smaller than T_r, the captured electron can be treated as quasifree. This means that REC can be described as capture of a free electron (radiative recombination - RR), which is the time inverse of photoionization. As the cross section for single photoionization can be calculated from the well known formula

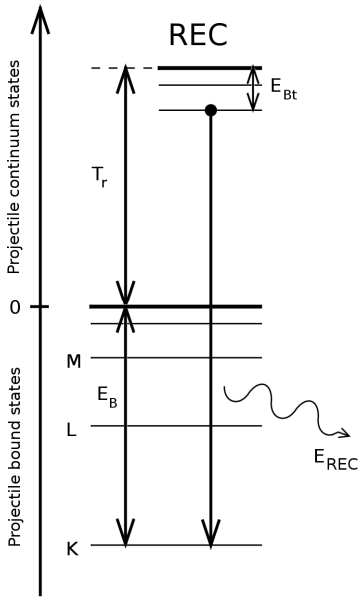


Figure 2.1: Radiative electron capture (REC). A target electron is captured into the projectile bound state and the energy excess is emitted as a single photon.

given by Stobbe [Sto 30], one can use it to calculate the REC cross section via the principle of detailed balance.

Principle of detailed balance describes the relation between the cross sections for direct ($\sigma_{i\to f}$) and time inverse ($\sigma_{f\to i}$) processes [Lan 79, Bey 03]:

$$g_i p_i^2 \sigma_{i\to f}(p_i) = g_f p_f^2 \sigma_{f\to i}(p_f), \tag{2.3}$$

where g is the number of possible states given by angular momentum and spin combinations and p is the momentum of the particle in the center of mass system describing the size of a phase space accessible for the initial (i) and final (f) states.

Based on Eq. 2.3 and the Stobbe formula for the photoionization cross section, the cross section for REC to the projectile K-shell during collision of a bare ion with a hydrogen target can be expressed in the form:

$$\sigma_{REC} = 9.16 \left(\frac{\nu^3}{1+\nu^2}\right)^2 \frac{\exp(-4\nu \cot^{-1}(1/\nu))}{1-\exp(-2\pi\nu)} \cdot 10^{-21}[cm^2], \tag{2.4}$$

where $\nu = Z_t e^2/\hbar v$ is the Sommerfeld parameter of the target K-shell electron and v is the projectile velocity. Thus, for fast collisions, the REC cross section scales with energy as:

$$\sigma_{REC} \sim \frac{Z_t Z^5}{v^5}. \tag{2.5}$$

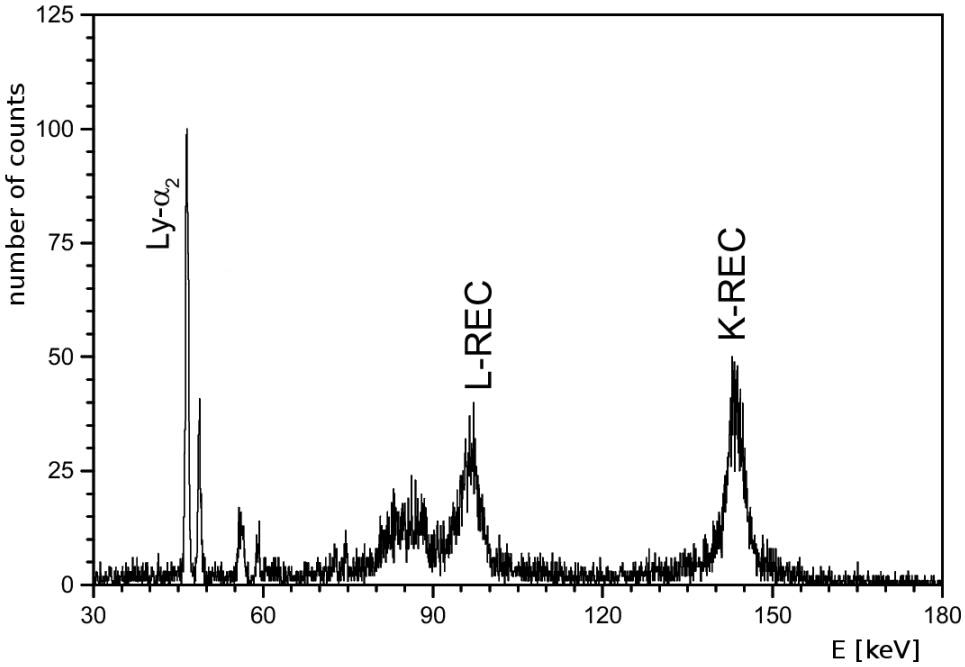


Figure 2.2: Example of the x-ray spectrum registered in coincidence with single electron capture during U^{92+} + N_2 collisions at 309.7 MeV/u [Swi 00].

When this result is compared with Eq. 2.1, one should notice that the radiative electron capture dominates for high energy collisions with light targets.

The angular distribution of the REC photons is given by the angular differential REC cross section calculated within the dipole approximation [Sch 72, Kie 73]:

$$\frac{d\sigma_{REC}}{d\Omega} = \frac{3}{8\pi}\sigma_{REC}\sin^2\vartheta. \tag{2.6}$$

Finally, the double differential cross section $d^2\sigma_{REC}/d\Omega dE_\gamma$ can be expressed as:

$$\frac{d^2\sigma_{REC}}{d\Omega dE_\gamma} = \frac{1}{v}\frac{d\sigma_{REC}}{d\Omega}\Big|_{p=p_0+p_z}\Im(p_z), \tag{2.7}$$

where $\Im(p_z)$ is the Compton profile of the target electrons. This formula describes the shape of the REC line registered within the x-ray spectrum at a given observation angle.

2.3 Bremsstrahlung

When a charged particle penetrates a gaseous or solid target a continuous x-ray spectrum is emitted. This spectrum is a result of bremsstrahlung processes occurring in the target

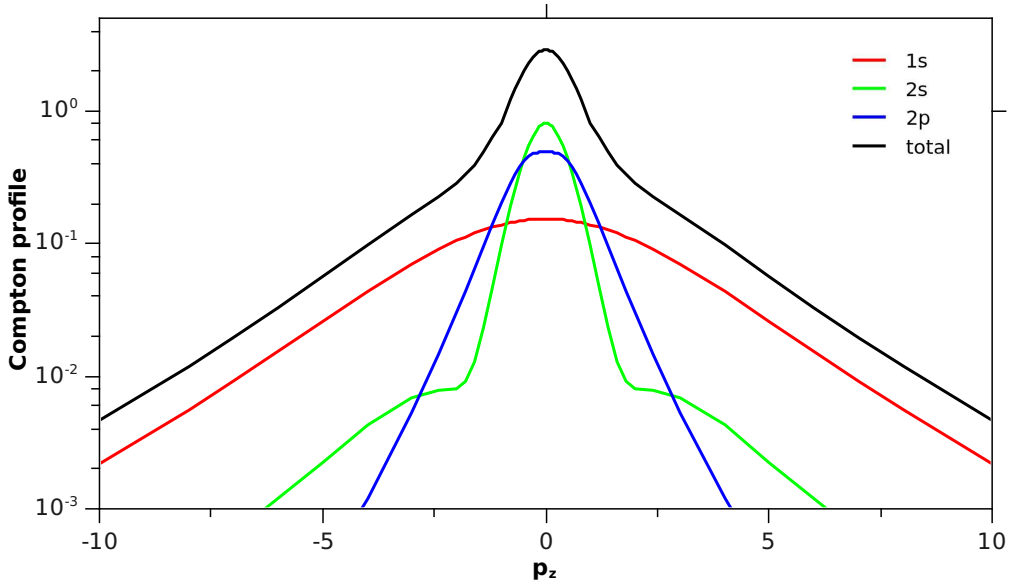


Figure 2.3: Compton profile of electrons in carbon atom. It can be noticed that the structure of the $1s$ line is much broader than that for $n = 2$ states [Big 75].

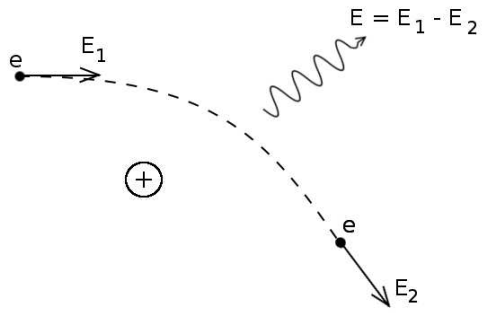


Figure 2.4: Example of the bremsstrahlung process for an electron in the electromagnetic field of an ion.

material, when a charged particle is accelerated (or decelerated) in the Coulomb field of the target components. A schematic explanation of this process for an electron in a field of an ion is presented in Fig. 2.4. Bremsstrahlung was first observed by Röntgen in 1895 [Roe 96, Roe 98] and since that time has been intensively studied [Ish 87, Ish 06, Mir 89, Chu 81, Jak 06, Lud 98].

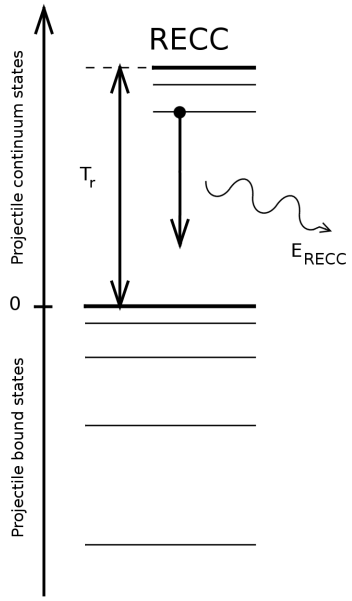


Figure 2.5: Radiative electron capture to continuum (RECC). Target electron is captured into a continuum state of the projectile and a photon is emitted.

During ion-atom collisions both the ion and ejected electrons may undergo bremsstrahlung processes. However, the total power radiated via bremsstrahlung is proportional to γ^4 (when $d\overrightarrow{v}/dt \perp \overrightarrow{v}$) or γ^6 (when $d\overrightarrow{v}/dt \parallel \overrightarrow{v}$) [Gri 01]. Since $E = \gamma mc^2$, where m is the rest mass of the moving particle, the total radiated power is proportional to $1/m^4$ or $1/m^6$, respectively. The above means that electrons lose energy via the bremsstrahlung process much more rapidly than heavier charged particles. This is why electron bremsstrahlung dominates over the ion-related processes.

Quasifree electron bremsstrahlung (QFEB), secondary electron bremsstrahlung (SEB), atomic bremsstrahlung (AB) and nucleus-nucleus bremsstrahlung (NB) dominate among various bremsstrahlung processes that can occur during ion-atom collision. These processes were taken into account during data analysis and are more thoroughly discussed in the following sections.

2.3.1 Electron bremsstrahlung

Radiative electron capture to continuum (RECC), sometimes referred to as quasi-free electron bremsstrahlung (QFEB), is a process where the target electron is captured to the

projectile continuum, which means it becomes a free electron. Energy conservation in this process is fulfilled by a photon emission (Fig. 2.5).

The maximum kinetic energy (T_r) of the involved electron, calculated in the projectile frame assuming $T_r \gg E_{Bt}$, is given by:

$$T_r = \frac{1}{2} m_e v^2 = \frac{m_e}{m_p} E, \tag{2.8}$$

where v is the velocity of the incoming ion in the laboratory frame (equal to the velocity of the captured electron in the projectile reference frame). T_r is the maximum energy (in the projectile frame of reference) of the photon emitted during the RECC process. As the maximum energy of the emitted photons is well defined, the spectrum of the emitted x-rays will have an edge at this value. This edge was observed, for example, during collisions of carbon ions with Be- and C-targets [Bed 98], as shown in Fig. 2.6.

Ejected target electrons may scatter in the Coulomb field of other target nuclei, producing additional bremsstrahlung. This process is referred to as secondary electron bremsstrahlung (SEB). In this case the maximum energy (T_m) of the emitted photons is equal to the maximum transfer of the kinetic energy during ion-electron collisions, given by:

$$T_m = 4T_r = 4\frac{m_e}{m_p} E. \tag{2.9}$$

Thus, similar to RECC, SEB spectrum has an edge at the photon energy of T_m [Ish 87].

During the atomic bremsstrahlung process (AB), the projectile excites a target electron to a target continuum state. This electron can be recaptured by a target atom with simultaneous emission of x rays. The electron can also lose only part of its energy but remain free, in which case this process is referred to as radiative ionization (RI).

It was shown in [Ish 06] that the relative contribution of the above processes strongly varies with projectile energy. The theoretical description of bremsstrahlung cross sections given in [Ish 06] is in agreement with experimental data. Comparison of experimental data for p + Al collisions at 1 and 4 MeV with theoretical calculations are presented in Fig. 2.7. Simple scaling formulae describing double differential bremsstrahlung cross sections were proposed in [Ish 06]:

$$\frac{(\hbar\omega)^2}{Z^2}\frac{d^2\sigma_{RECC}}{d(\hbar\omega)d\Omega} = Z_t f(\frac{m_e}{m_p}\frac{E}{\hbar\omega}), \tag{2.10}$$

$$\frac{(\hbar\omega)^3}{Z^2}\frac{d^2\sigma_{AB}}{d(\hbar\omega)d\Omega} = f(\frac{a_0\omega}{v_p}), \tag{2.11}$$

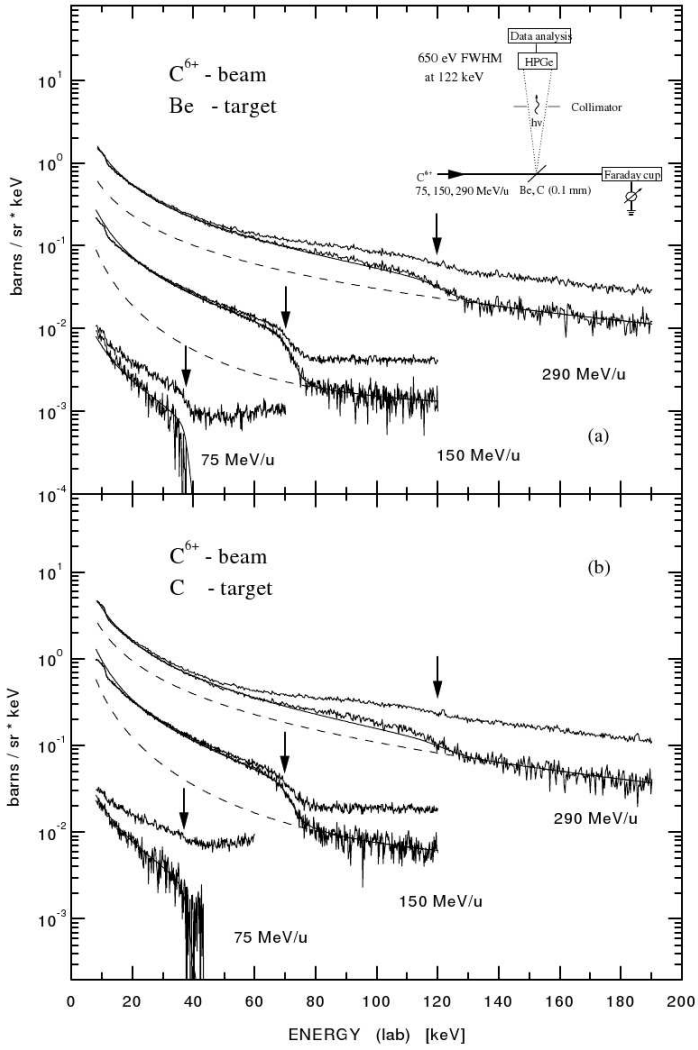


Figure 2.6: Spectra observed during the experiment of [Bed 98] for: (a) Be-target, (b) C-target. For each energy-target combination two spectra are displayedwith the upper spectrum showing the raw data and the lower spectrum with the results after background subtraction. For presentation purposes spectra were multiplied by factors; (a) Be-target: 1/20 for 75 MeV/u, 10 for 290 MeV/u; (b) C-target: 1/8 for 75 MeV/u, 10 for 150 MeV/u, 50 for 290 MeV/u. Dashed line: SEB contribution, solid line: RECC (relativistic approximation) + K-REC + SEB. Arrows show the RECC-edge energy T_r transformed to the laboratory frame. Inset in (a) represents the experimental setup.

$$\frac{(\hbar\omega)^2}{Z^2}\frac{d^2\sigma_{SEB}}{d(\hbar\omega)d\Omega} = Z_t^2 f(\frac{m_e}{m_p}\frac{E}{\hbar\omega}). \tag{2.12}$$

where $\hbar\omega$ denotes photon energy, a_0 is the Bohr radius and f is a universal function discussed extensively in [Ish 06]. The bremsstrahlung processes for protons interacting with various targets at a wide range of energies were thoroughly studied for example by Folkmann [Fol 84,

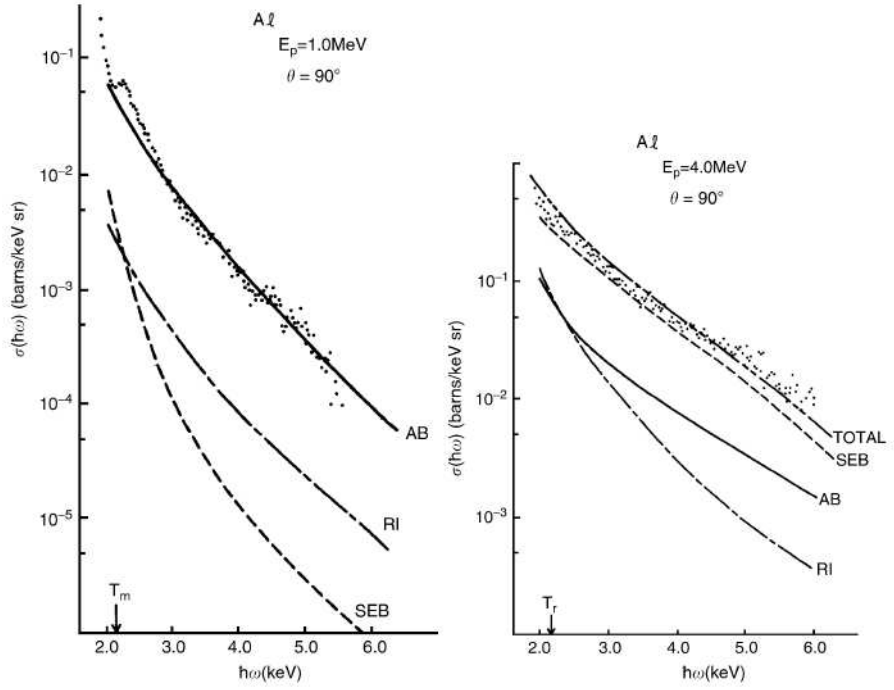


Figure 2.7: Example of the contribution of various bremsstrahlung processes to the continuous x-ray spectrum during pl + Al collisions at 1 and 4 MeV [Ish 06]. It can be noticed that SEB becomes a dominating process at higher beam energy.

Fol 75]. By means of the above formulae, the bremsstrahlung contribution to the experimental data can be estimated from the proton data.

2.3.2 Nucleus-nucleus bremsstrahlung (NB)

Nucleus-nucleus bremsstrahlung is a consequence of the projectile scattering in the Coulomb field of the target nuclei. The emitted x-ray spectrum extends up to the projectile energy. The differential cross section for NB process can be calculated from the formula given by Mokler [Mok 78]:

$$\frac{d\sigma_{NB}}{d(\hbar\omega)} = C\frac{Z^2 Z_t^2}{(\hbar\omega)E} A \left(\frac{Z}{A} - \frac{Z_t}{A_t}\right)^2, \tag{2.13}$$

$$C = \ln\left(\frac{\left(1+\sqrt{1-x}\right)^2}{x}\right) \cdot 4.3 \cdot 10^{-28}[cm^2], \tag{2.14}$$

$$x = \frac{A + A_t}{A_t}\frac{(\hbar\omega)}{E}, \tag{2.15}$$

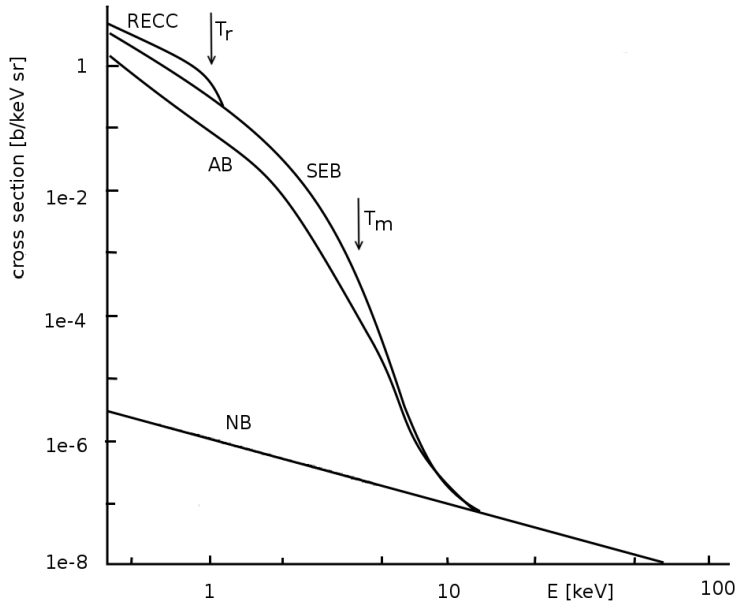


Figure 2.8: Bremsstrahlung processes observed during p + C collisions at 2 MeV. Plot based on Fig. 3 in [Ish 06].

where A, A_t are projectile and target masses in atomic units, respectively.

Fig. 2.8 shows the contribution of RECC, SEB, AB and NB to the x-ray spectra obtained during collisions of 2.0 MeV protons with carbon. Upper limits of RECC and SEB x-ray spectra can be observed at T_r and T_m, respectively. The NB cross section is significantly lower than those of the electron bremsstrahlung processes. Thus, NB plays a significant role only within the x-ray spectrum range above T_m.

2.4 Multielectron capture processes, noncorrelated double radiative electron capture (DREC)

During a single ion-atom collision capture of more than one target electron to the projectile bound state is possible. The simplest example of a noncorrelated capture of two electrons is double radiative electron capture (DREC) for which the capture of two electrons is accompanied by the emission of two independent REC photons (Fig. 2.9). During this process the captured electrons do not interact with each other and the capture of each of them can be treated as a separate process.

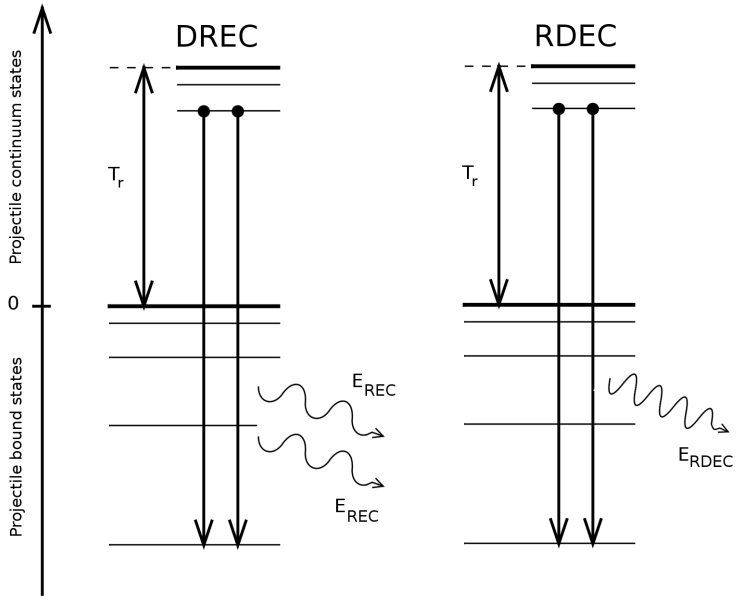


Figure 2.9: Comparison of the DREC and RDEC processes.

Radiative noncorrelated double capture was theoretically addressed by Meyerhof [Mey 85]. In this paper the author calculated the REC cross section as an integral of the process probability given as a function of impact parameter. The single electron capture cross section can be calculated as an integral of the probability $P(b)$ of an electron capture given as a function of the impact parameter b:

$$\sigma_{REC} = \int_0^\infty db 2\pi b P(b). \tag{2.16}$$

In case of REC, $P(b)$ is given by:

$$P(b) = \sigma_{REC}(Z_t = 1) \int_{-\infty}^{\infty} dz \rho(R), \tag{2.17}$$

R being the projectile to target atom distance and ρ the electron density. As the electron density is normalized:

$$\int_0^\infty db 2\pi b \int_{-\infty}^{\infty} dz \rho(R) = Z_t, \tag{2.18}$$

the REC cross section for a multielectron target is simply given by $Z_t \sigma_{REC}(Z_t = 1)$.

The same method was applied to noncorrelated double radiative capture. If $P_0(b)$ is the probability of a single electron capture into the bare ion, and $P_1(b)$ is the corresponding probability of electron capture into the H-like ion, the cross section for noncorrelated double

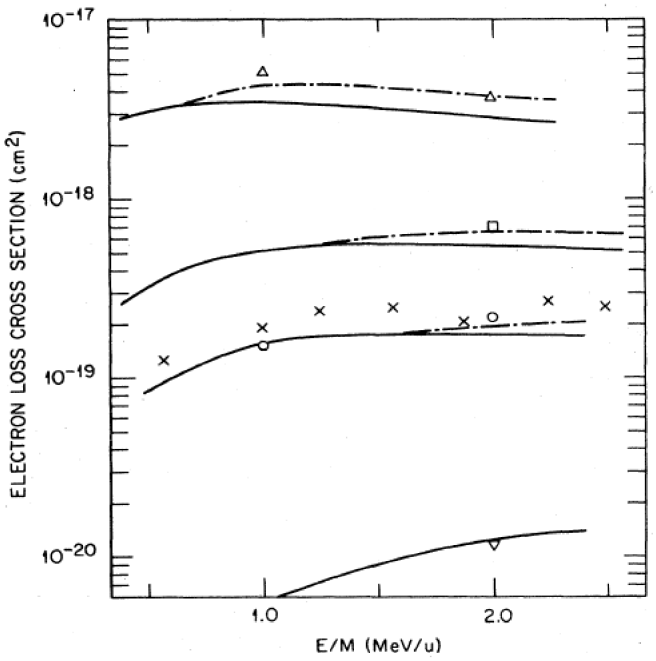


Figure 2.10: Single electron loss cross section as given in [Hip 87]. Solid line: PWBA calculations for He^{2+} impact, dot-dashed line: includes contribution from free electron impact in CBE approximation. Symbols: $\triangle$ – Si^{8+}, $\square$ – O^{6+}, $\triangledown$ – Si^{13+}, $\circ$ and $\times$ – O^{7+}.

electron capture can be expressed as [Mey 85]:

$$\sigma_{DREC} = \int_0^\infty db 2\pi b P_0(b) P_1(b). \tag{2.19}$$

For double electron capture (DREC) one obtains the cross section [Mey 85]:

$$\sigma_{DREC} = 0.13 Z_t^{1/2} \sigma_{REC}^2(Z_t) a_0^{-2}. \tag{2.20}$$

The above formula was verified experimentally by Bednarz [Bed 03].

When the captured electrons interact with each other during the collision, the process is referred to as correlated capture. Radiative double electron capture (RDEC) is the basic example of a correlated process and can be treated as a time inverse of double photoionization. Thus, due to the electron-electron interaction of the two captured electrons only one photon is emitted and its energy is about two times greater than that of a single REC photon (Fig. 2.9). The RDEC process is discussed in detail in Chapter 3.

2.5 Projectile ionization – electron loss

There is a variety of terminology used in the literature when reffering to electron detachment, which leads to confusion. Here, a nomenclature from [Bom 89, Tan 91, Hip 87] is applied. The term ionization is used when the electron is detached from the target atom, while the removal of the electron from the projectile bound state is reffered to as electron loss. Consequently, electron loss is the process where an electron is removed from the projectile and remains free afterwards:

$$A^{q+} + A_t \rightarrow A^{(q+x)+} + A_t + xe^-, \tag{2.21}$$

where x is the number of electrons lost by the projectile ($q + x \leq Z$). Electron loss processes have been extensively studied during the late seventies and eighties for various elements and charge states within energy range up to 10 MeV/u [Gra 84, Gra 85, Ols 78].

Boman et al. [Bom 89] developed a simple scaling formulae for electron loss cross section. The single electron loss cross section for oxygen ions at 1 MeV/u can be estimated as:

- for $q = 5$:

$$\sigma_1^5 = (3.27 \cdot 10^{-18}) Z_t^{0.98} [cm^2], \tag{2.22}$$

- for $q = 6$:

$$\sigma_1^6 = (8.83 \cdot 10^{-19}) Z_t^{0.78} [cm^2], \tag{2.23}$$

- for $q = 7$:

$$\sigma_1^7 = (2.22 \cdot 10^{-19}) Z_t^{0.33} [cm^2], \tag{2.24}$$

where q denotes the initial charge state of the ion. It has been also checked by the authors that in case of Si^{8+} + He collisions at 1.0 MeV/u the ratio of single to double electron loss cross sections $\sigma_1^8/\sigma_2^8 \approx 40$. Thus, it can be assumed that the double electron loss process can be neglected for the case of the more tightly bound K-shell electrons in O^{6+}. As can be observed in Fig 2.10 the single electron loss cross section does not change significantly when the beam energy is increased from 1 to 2 MeV/u. Thus, the scaling formulae given by Eqs 2.22-2.24 can be used to estimate the cross sections within this energy range.

Chapter 3

Radiative double electron capture (RDEC)

Radiative double electron capture (RDEC) is a one-step process for which two free (or quasifree) target electrons are captured into bound states of the projectile, e.g. into an empty K-shell, and the energy excess is released as a single photon (Fig. 2.9). This process has to be compared with a two-step double radiative electron capture (DREC) during which two electrons are captured independently and two single REC photons are emitted.

While for the DREC process both electrons can be treated separately (see Section 2.3.2), in case of the RDEC one has to go beyond the independent electron model. Here, due to the electron-electron interaction, transitions of two target electrons into the projectile bound states occur with an emission of one photon with an energy about two times greater than that of a single DREC photon.

In general, captured electrons may originate from two different orbitals in the target and arrive finally at different final states in the projectile. Thus, the energy of the RDEC photon can be expressed as:

$$E_{RDEC} \approx 2T_r + E_B^{(1)} + E_B^{(2)} - E_{Bt}^{(1)} - E_{Bt}^{(2)} + \overrightarrow{v}\overrightarrow{p}^{(1)} + \overrightarrow{v}\overrightarrow{p}^{(2)}, \tag{3.1}$$

where the indices (1) and (2) correspond to each of the captured electrons. The width of the peak is about twice as large as that of the REC line. Roughly, it is determined by the sum of Compton profiles of the two active electrons [Mir 89].

3.1 Initial experiments dedicated to RDEC

The first experiment dedicated to RDEC was performed at GSI in 1994 with 11.4 MeV/u Ar^{18+} ions from the UNILAC impinging upon a carbon foil. A detailed description of this

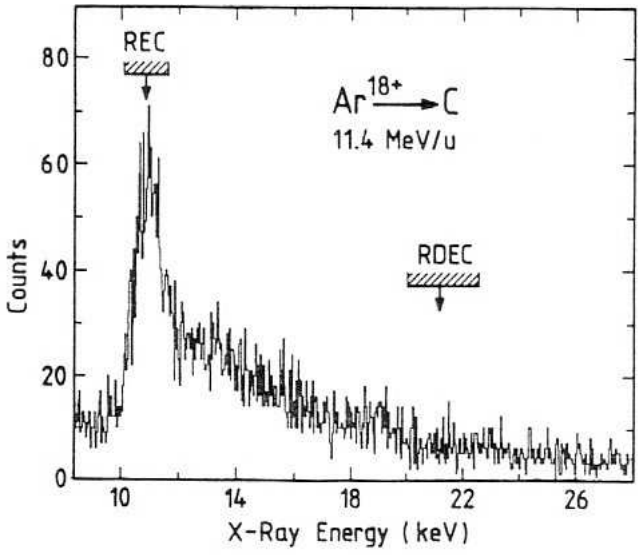


Figure 3.1: Typical x-ray spectrum obtained during argon experiment [War 95].

experiment is given in [War 95]. A typical spectrum obtained during that experiment is presented in Fig. 3.1. As shown in this figure, no significant line structure related to the RDEC process was observed. However, the number of counts collected in the expected RDEC energy window provided an upper limit of the RDEC cross section of about 5.2 mb. A rough theoretical estimate of the cross section ratio $\sigma_{RDEC}/\sigma_{REC}$ was also suggested, based on the principle of detailed balance and considering REC as a time reversal of photoionization. The REC and RDEC cross sections can be written as:

$$\sigma_{REC}(\beta) = Z_t \left(\frac{\hbar\omega}{\gamma\beta mc^2}\right)^2 \sigma_{PI}(\hbar\omega), \tag{3.2}$$

$$\sigma_{RDEC}(\beta) = FZ_t(Z_t-1) \left(\frac{\hbar\omega'}{2\gamma\beta mc^2}\right)^2 \sigma_{DPI}(\hbar\omega'), \tag{3.3}$$

where σ_{PI} and σ_{DPI} are the cross sections for single and double photoionization, respectively. The factor F ($F \leq 1$) describes the phase space fraction of double photoionization accessible for the RDEC process. Thus, the $\sigma_{RDEC}/\sigma_{REC}$ ratio can be expressed in terms of single and double photoionization cross sections as [War 95]:

$$R = \frac{\sigma_{RDEC}}{\sigma_{REC}} = F(Z_t-1) \left(\frac{\omega'}{2\omega}\right)^2 \left(\frac{\sigma_{DPI}(\hbar\omega')}{\sigma_{PI}(\hbar\omega)}\right), \tag{3.4}$$

or, as in case of RDEC $\hbar\omega' \approx 2\hbar\omega$:

$$R = \frac{\sigma_{RDEC}}{\sigma_{REC}} = F(Z_t-1)\frac{\sigma_{PI}(2\hbar\omega)}{\sigma_{PI}(\hbar\omega)}\frac{\sigma_{DPI}(2\hbar\omega)}{\sigma_{PI}(2\hbar\omega)}. \tag{3.5}$$

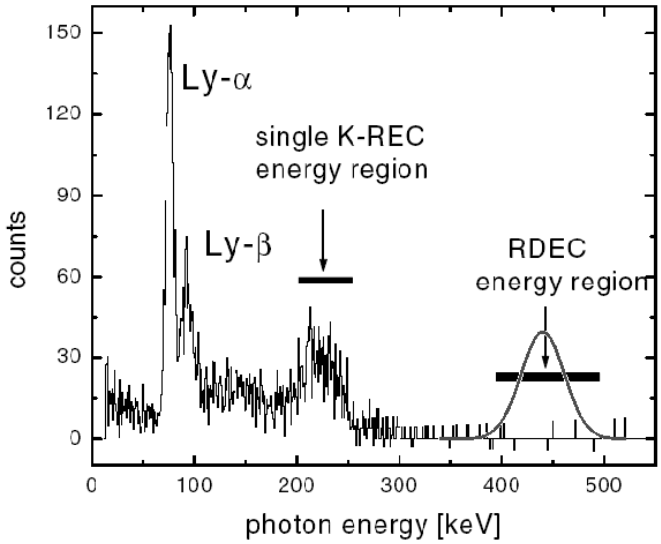


Figure 3.2: Typical experimental x-ray spectrum obtained for uranium ions [Bed 03]. The Gaussian solid line shows the expected RDEC peak, which should be observed according to Yakhontov et al. [Yak 96, Yak 97].

where the values of the expresssions: $\sigma_{PI}(2\hbar\omega)/\sigma_{PI}(\hbar\omega)$ and $\sigma_{DPI}(2\hbar\omega)/\sigma_{PI}(2\hbar\omega)$ can be easily estimated from [Fan 59, Amu 75]. The experiment [War 95] provided an upper limit for R of $3.1 \cdot 10^{-6}$.

This experiment stimulated theoretical treatment of the RDEC process [Yak 96, Yak 97]. In these papers the authors presented nonrelativistic calculations of the RDEC process adapted to the kinematics and the energy range of the Ar^{18+} + C experiment. The calculations gave, for this particular collision system (Ar^{18+} + C at 11.4 MeV/u), the RDEC to REC cross section ratio R of $3.6 \cdot 10^{-6}$, which is close to the experimental upper limit.

Moreover, these calculations predicted a strong enhancement of RDEC during heavy ion-atom collisions at relativistic energies [Yak 97]. These calculations were tested during the second experiment dedicated to RDEC. Here, bare uranium ions at an energy of 297 MeV/u collided with an Ar target at the ESR storage ring of the GSI facility [Bed 03]. This experiment showed that for the collision system under consideration the RDEC cross section is certainly at least three orders of magnitude smaller than the theoretical prediction [Yak 96, Yak 97]. Fig. 3.2 shows a spectrum obtained during the experiment. Again, no significant line structure which could be assigned to the RDEC process was observed. The Gaussian line in Fig. 3.2 shown within the RDEC region of the spectrum represents the shape of the RDEC line which

should be observed in the spectrum, if the theoretical calculations [Yak 96, Yak 97] were reliable. This experiment also provided only an upper limit for the RDEC cross section value of about 10 mb.

3.2 Recent theoretical approach to RDEC

In order to explain the disagreement between the uranium experiment [Bed 03] and the theoretical treatment of RDEC [Yak 96, Yak 97], a new theoretical approach for the correlated double electron capture into the K-shell of bare ions was proposed [Mik 04a, Mik 04b, Nef 05]. Here, a brief description of this RDEC treatment is given with the notation used in the original papers. Indices (1) and (2) correspond to REC and RDEC, respectively, and natural units ($\hbar = c = 1$) are used throughout the text.

All the electrons involved in the process were considered as nonrelativistic and the energy ω of the emitted photon was limited by $I_{2K} \leq \omega \ll m$, where I_{2K} is the threshold energy for double photoionization of the projectile K-shell and m is the electron mass. In such case the Coulomb parameter (αZ, α denotes the fine structure constant) is small ($\alpha Z \ll 1$) and perturbation theory with respect to the electron-electron interaction can be used.

In the reference frame of the incident ion the probability dW for double electron capture into the K-shell of bare ion with the emission of a single photon per unit time is given by [Mik 04a]:

$$dW = \frac{2\pi}{V^2}|A|^2 \frac{d\overrightarrow{k}}{(2\pi)^3}\delta(2E_P - \omega - I_{2K}), \tag{3.6}$$

where E_P is the one-electron energy within the initial continuum state, $\omega = |\overrightarrow{k}| = k$ is the energy of the emitted photon and $I_{2K} = 2I$ with $I = \eta^2/2m$, the Coulomb potential for single ionization and $\eta = m\alpha Z$ the characteristic momentum of the K-shell electron, and V is a normalization factor. Summation over all polarizations of the emitted photon is assumed in Eq. 3.6 and the delta function ensures energy conservation. The amplitude A was obtained from that for the double K-shell photoionization. A detailed description of this approach is given in [Mik 04a].

Dividing Eq. 3.6 by the current flux of the incident target electrons $j = v/V$, where $v = p/m$ is the absolute value of the initial velocity of the incident electrons before collision with the ion, one obtains the effective differential cross section:

$$d\sigma^{(2)} = 2\pi \frac{\omega^2}{vV}|A|^2 \frac{d\Omega_k}{(2\pi)^3}, \tag{3.7}$$

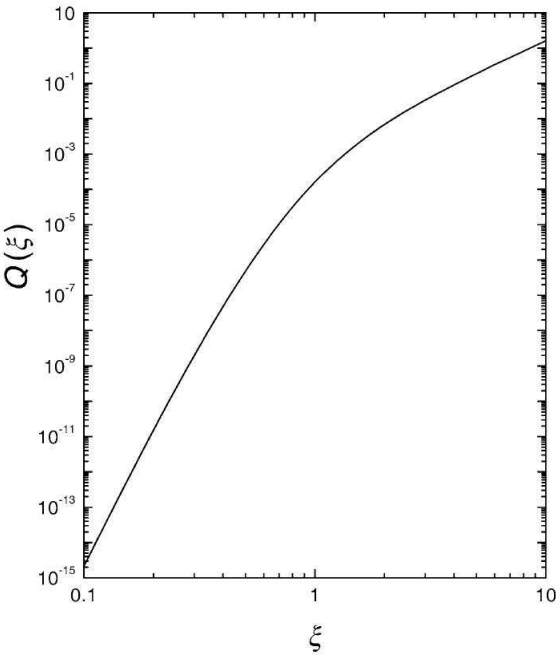


Figure 3.3: Universal function Q calculated as a function of the dimensionless variable ξ [Mik 04a].

which defines the angular distribution of the RDEC photons emitted into an element of a solid angle $d\Omega_k$.

For the energy regime assumed in these calculations, it was possible to calculate the total cross sections within the electric dipole approximation. For collisions of heavy ions with light target atoms the total cross section for radiative double electron capture (RDEC) into the K-shell of the ion is given by:

$$\sigma^{(2)} = \frac{2^{19} Z_t^3}{3\pi Z^5} Q(\xi), \tag{3.8}$$

where $\xi = \eta/p$ is a dimensionless parameter, $\sigma_0 = \alpha^3 a_0^2$ and a_0 denotes the Bohr radius. Q is a universal function of ξ, which can be obtained by numerical integration (Fig. 3.3). $\xi \sim 1$ corresponds to the near-threshold domain, where the K-shell photoeffect reaches its maximum. For slow collisions ($\xi \gg 1$) the RDEC cross section increases, while in case of fast collisions it decreases rapidly. Moreover, it has to be pointed out that the RDEC cross section rapidly drops with the projectile atomic number ($\sim Z^{-5}$) and increases significantly for low energy collisions.

Another value calculated in [Mik 04a] is the cross section ratio ($R = \sigma^{(2)}/\sigma^{(1)}$). The REC cross section can be expressed in terms of the photoionization cross section (σ_{PI}) via

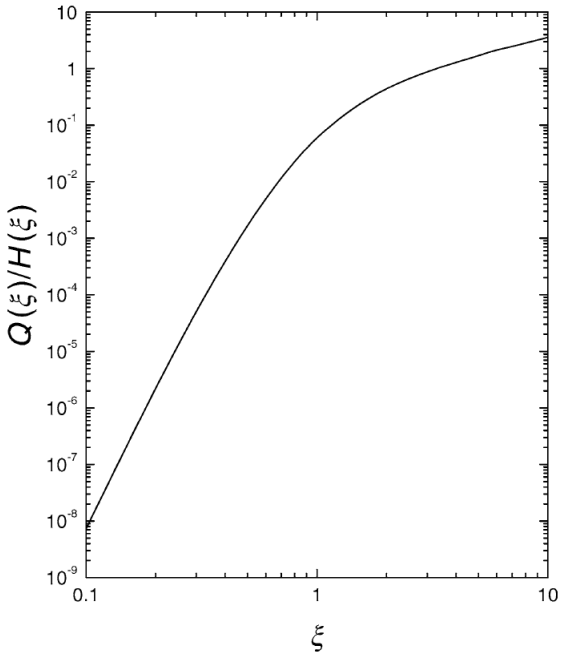


Figure 3.4: Universal quantity Q/H calculated as a function of the dimensionless variable ξ [Mik 04a].

the principle of detailed balance. As σ_{PI} is known analytically (Stobbe formula [Sto 30]), for radiative electron capture into the K-shell of the projectile one obtains:

$$\sigma^{(1)} = \frac{2^{10}}{3}\pi^2\sigma_0 Z_t H(\xi), \tag{3.9}$$

$$H(\xi) = \frac{\xi^2}{\varepsilon_\gamma^2}\frac{\exp(-4\xi\cot^{-1}\xi)}{1-\exp(-2\pi\xi)}, \tag{3.10}$$

where $\varepsilon_\gamma = \omega/I = 2(1+\xi^{-2})$ is the dimensionless photon energy. Then the ratio R is given by:

$$R = \frac{2^9 Z_t^2 Q(\xi)}{\pi^3 Z^5 H(\xi)}. \tag{3.11}$$

The function $Q(\xi)/H(\xi)$ is presented in Fig. 3.4.

These calculations are in disagreement with the previous relativistic approach [Yak 97], which was not able to explain the existing experimental data [Bed 03]. As shown in [Mik 04a], the enhancement of the wave function for the relativistic systems was calculated incorrectly by Yakhontov [Yak 97] and even the corrected value, which is 3 orders of magnitude smaller [Mik 04a], was not confirmed by the experiment [Bed 03]. Therefore, the enhancement of the RDEC cross section for relativistic systems [Yak 97] seems to be absent. This is similar to

Table 3.1: Comparison of experimentally obtained RDEC cross sections [War 95, Bed 03] and the calculated values given in [Yak 97] and [Mik 04a].

Z	E [MeV/u]	ξ	Z_t	$\sigma^{(2)}$ [mb]		
				Ref. [Mik 04a]	Ref. [Yak 97]	experiment
18	11.4	0.840	6	3.2	1.85	$\leq$5.2 [War 95]
92	297	0.841	18	$2.5{\cdot}10^{-2}$	5000	$\leq$10 [Bed 03]

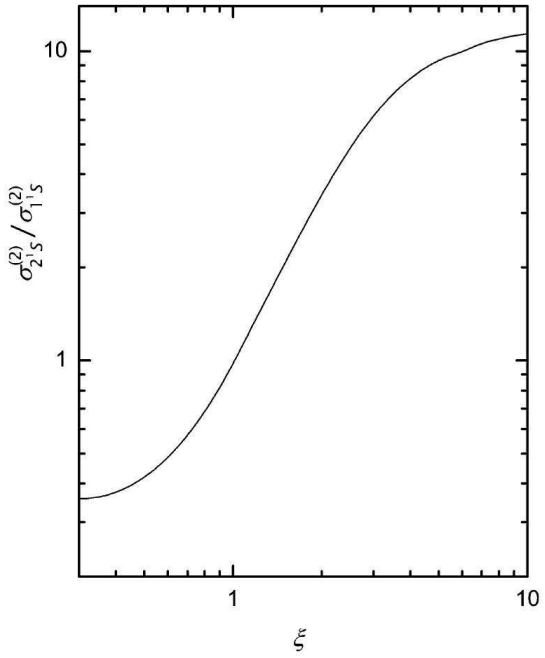


Figure 3.5: The ratio of the RDEC cross sections to the excited ($\sigma^{(2)}_{2^1S}$) and ground ($\sigma^{(2)}_{1^1S}$) projectile states as a function of adiabacity parameter ξ [Nef 05].

the behavior of the cross section for the REC process, where the cross section decreases when the projectile energy increases.

However, it has to be emphasized that the current estimate [Mik 04a] of $\sigma^{(2)}$ gives values closer to the experimentally obtained upper limits for both the nonrelativistic case (Ar^{18+} + C, [War 95]) and the relativistic one (U^{92+} + Ar, [Bed 03]) (see Table 3.1), which suggests that [Mik 04a] is so far the most reliable theoretical description of RDEC.

In contradiction to predictions given in [Yak 97], the new calculations show that the RDEC cross section strongly depends on the target atomic number and electron density. One can

Table 3.2: The REC ($\sigma^{(1)}$), RDEC ($\sigma^{(2,\gamma)}$) and DREC ($\sigma^{(2,2\gamma)}$) cross sections and their ratios as given in [Dru 07].

Z	ξ	E [MeV/u]	Z_t	$\sigma^{(1)}$ [kb]	$\sigma^{(2,2\gamma)}$ [mb]	$\sigma^{(2,\gamma)}$ [mb]	$\sigma^{(2,\gamma)}/\sigma^{(1)}$	$\sigma^{(2,\gamma)}/\sigma^{(2,2\gamma)}$
	0.84	11.4		0.36	1.5	3.2	$8.9{\cdot}10^{-6}$	2.1
18	0.20	646	6	$1.5{\cdot}10^{-3}$	$2.6{\cdot}10^{-5}$	$1.0{\cdot}10^{-6}$	$6.7{\cdot}10^{-10}$	$3.2{\cdot}10^{-2}$
	0.10	804		$6.4{\cdot}10^{-5}$	$4.7{\cdot}10^{-8}$	$1.6{\cdot}10^{-10}$	$4.0{\cdot}10^{-12}$	$3.4{\cdot}10^{-3}$
	0.84	5.1		0.36	1.5	24	$6.7{\cdot}10^{-5}$	16
12	0.20	287	6	$1.5{\cdot}10^{-3}$	$2.6{\cdot}10^{-5}$	$7.6{\cdot}10^{-6}$	$5.1{\cdot}10^{-9}$	0.29
	0.10	357		$6.4{\cdot}10^{-5}$	$4.7{\cdot}10^{-8}$	$1.2{\cdot}10^{-9}$	$1.9{\cdot}10^{-11}$	$2.6{\cdot}10^{-2}$

expect much larger values of $\sigma^{(2)}$ in case of slow collisions of multicharged ions with a solid state target with low atomic number Z_t [Mik 04a]. As the orbital velocity of the target valence electrons is much smaller than that of the projectile, they can be considered as quasifree in the projectile's frame of reference. In this reference frame these electrons appear as an electron beam with velocity v and concentration $n_e = \kappa\rho_t N_A/M_t$, where κ is the number of valence electrons, N_A is Avogadro's number and ρ_t and M_t are the density and molar mass of the target, respectively. Hence, by substituting $V = n_e^{-1}$ in Eq. 3.7 $\sigma^{(2)}$can be expressed as:

$$\sigma^{(2)} = (n_e a_0^3)\frac{2^{19}\sigma_0}{3Z^5}Q(\xi). \tag{3.12}$$

In addition, the correlated double electron capture into the $1s2s$ state increases the cross section for the RDEC process [Nef 05]. As shown in Fig. 3.5, the ratio of the cross section for RDEC to the $1s2s$ state, $\sigma^{(2)}_{2^1S}$, to the cross section for RDEC to the $1s^2$ ground state, $\sigma^{(2)}_{1^1S}$, is strongly dependent on the ξ value. As can be seen from Fig. 3.5, for $\xi \gg 1$ (i.e. slow collisions) the cross section for electron capture to the $1s2s$ state can greatly exceed that for $1s^2$ state capture.

Recently, the calculations of Nefiodov and Mikhailov were continued by Drukarev [Dru 07], who again addressed the high energy nonrelativistic limit ($\xi \gg 1$) of the RDEC process. As previously found, a strong energy dependence of the cross section was shown and the RDEC probability was compared with the one for noncorrelated capture. Obtained values of the REC, RDEC and DREC cross sections for Ar^{18+} + C and Mg^{12+} + C for various projectile energies are given in Table 3.2.

This theory [Mik 04a, Mik 04b, Nef 05, Dru 07] suggests that the best systems for observation of the RDEC process are low energy collisions of mid-Z ions with light solid targets.

This theory was a motivation for the next RDEC experiment and a reason for the choice of the conditions of the experiment presented in this thesis.

Chapter 4

Experimental setup at Western Michigan University

4.1 Van de Graaff accelerator

The Van de Graaff accelerator is an electrostatic generator which uses a moving belt to accumulate very high, electrostatically stable voltage on a hollow metal sphere [Gra 47]. This type of generator was developed by Robert J. Van de Graaff at Princeton University. The first model was demonstrated in October 1929 and in 1931 a version able to produce a potential difference of 1 MV was described [Gra 31].

A simple Van de Graaff generator is presented in Fig. 4.1. A belt of dielectric material runs over two rollers, one of which is surrounded by a hollow metal sphere the high voltage terminal. Two electrodes, an upper and a lower one, are placed next to each roller. The upper electrode is connected to the sphere, while a high DC potential (with respect to the ground potential) is applied to the lower one, a positive potential in the example.

Due to the strong electric field the air around the lower electrode is ionized and the positive ions are repelled from the electrode and accumulated on the belt. Then they are transported towards the upper electrode which collects the charges from the belt and transports them onto the spherical collecting electrode. The potential of the HV electrode increases until the speed of its charging equals the speed of discharging. The maximum potential obtained on the HV electrode depends on the radius of the sphere and insulating properties of the gases surrounding it. SF_6 or a mixture of N_2 and CO_2 under a pressure even up to 20 bar are usually used [Hin 97]. The value of the terminal voltage in Van de Graaff accelerators may reach up to 15-20 MV [Edw 93, Bey 03].

If a source of positive ions is placed close to the high voltage terminal, as in Fig. 4.1, the ions are repelled by the positive charge of the terminal electrode and thus accelerated towards

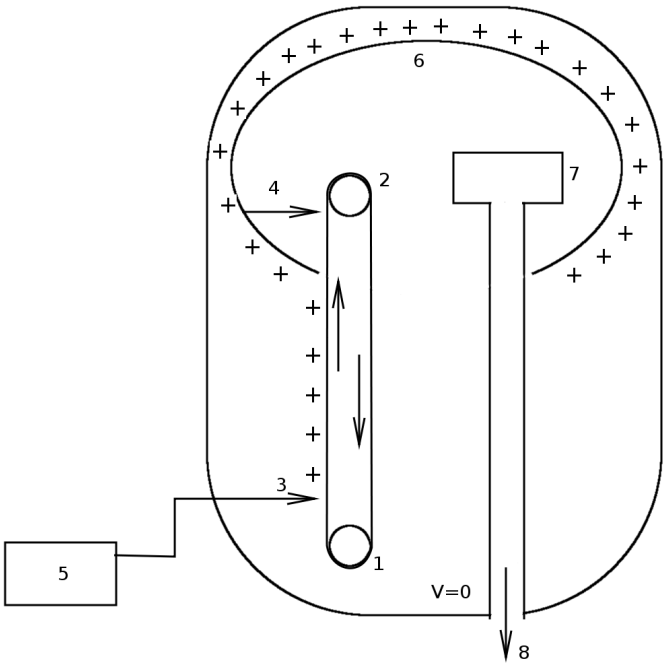


Figure 4.1: Schematic view of a classical Van de Graaff accelerator: (1) lower roller, (2) upper roller, (3) charging electrode, (4) electrode collecting positive charge, (5) voltage generator, (6) spherical electrode (high voltage terminal), (7) ion source, (8) extracted ion beam.

the ground potential. The final kinetic energy of the ions depends on their charge state q and is proportional to the terminal voltage $V_{terminal}$:

$$E = qV_{terminal}. \tag{4.1}$$

In modern ion accelerators with a Van de Graaff generator, electrodes located at entry and exit of the vacuum tube are grounded and the high-voltage terminal is located at the middle of the tube, as shown in Fig. 4.2 [Hin 97, Wed 99]. A source of negative ions is placed at the entrance of the tube and produced ions, usually singly charged, are accelerated within the tube towards the high-voltage terminal, where two or more electrons are removed from each ion as it passes through a stripping foil. The charge state of the ion changes from negative to positive and the ion is repelled from the terminal and accelerated towards the grounded exit of the tube. Compared to Van de Graaff accelerators of the ordinary type, by means of tandem Van de Graaff accelerators higher particle energies can be obtained since the potential difference is used for the acceleration twice. Thus, in this case the final kinetic energy can be

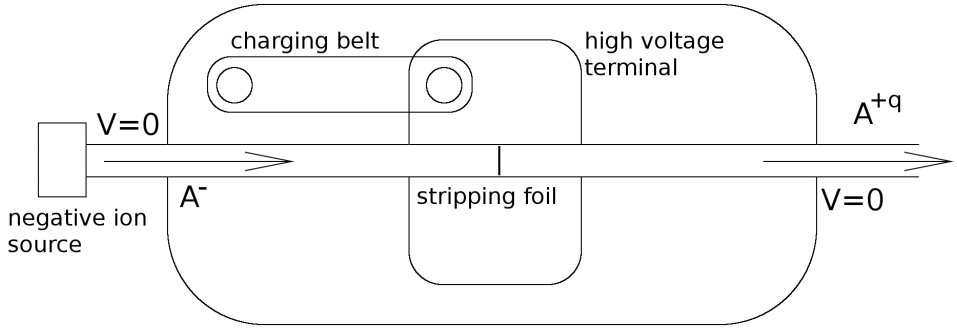


Figure 4.2: Schematic view of a tandem Van de Graaff accelerator: A negative ion entering the accelerator (A^-) is accelerated by the high terminal voltage. Some of its electrons are removed while the ion passes through the stripping foil. The positive ion (A^{+q}) is repelled by the high voltage terminal, thus causing additional acceleration.

calculated as:

$$E = (q + 1)V_{terminal}, \tag{4.2}$$

where q is the ion charge state after passing through the stripping foil.

The experiment described in this dissertation was performed at Western Michigan University using 6 MV tandem Van de Graaff accelerator. The WMU accelerator was built by the High Voltage Engineering Corporation, the company founded by Robert Van de Graaff. The construction of the accelerator allows for obtaining stable beams of bare ions of all elements up to ^{9}F with a total kinetic energy up to 40 MeV.

4.2 Beam line setup at Western Michigan University

A schematic view of the WMU accelerator beam line is presented in Fig. 4.3. The accelerated beam passes through a 90° analyzing magnet which allows for choosing the appropriate ion charge state. At this point, the final energy of the beam is defined accordingly to Eq. 4.2. Then the beam passes through a post stripper followed by a switching magnet which directs the desired charge state towards the experimental area. For the presented experiment a beam of O^{6+} was extracted from the accelerator operating at the terminal voltage of 5.43 MV, which produced a beam of energy equal to 38 MeV. Then the beam traversed through a 20 μg/cm^2 carbon stripper foil, where bare and H-like oxygen ions were produced. Simply, by

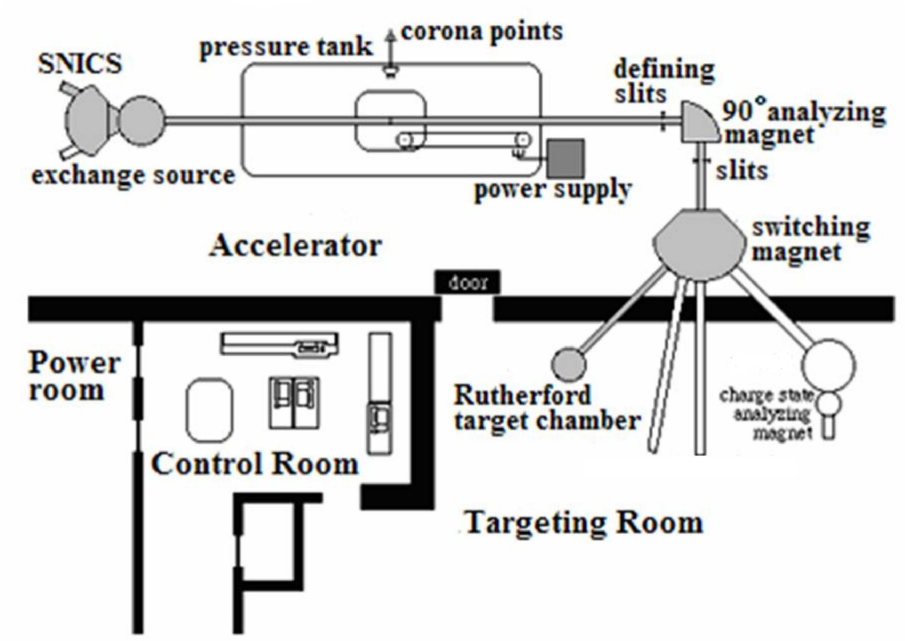


Figure 4.3: Schematic view of the WMU van de Graaff accelerator facility [Kay].

changing the magnetic field of the switching magnet one could choose the necessary charge state. When a proton beam was accelerated, the post-stripper was removed from the beam line.

The experimental beam line farthest left, when looking along beam direction, was used during this experiment. There, an exclusively designed chamber for a solid target was placed, which not only allowed for mounting up to four films but also provided a simple mechanism for target rotation. This was necessary for optimization of the target position during the experiment. During data acquisition the target film was positioned at 45° to the beam direction, facing the x-ray detector as shown in Fig. 4.4. This setup ensured a direct detection of emitted photons, as they did not traverse through the foil, so the unnecessary energy loss was avoided. It also allowed for usage of the whole active area of the x-ray detector, which was not covered by the aluminum frame of the target holder. The target foils used during the experiment were a few μg/cm^2 thick which corresponds to an areal density on the order of 10^{17} particles/cm^2.

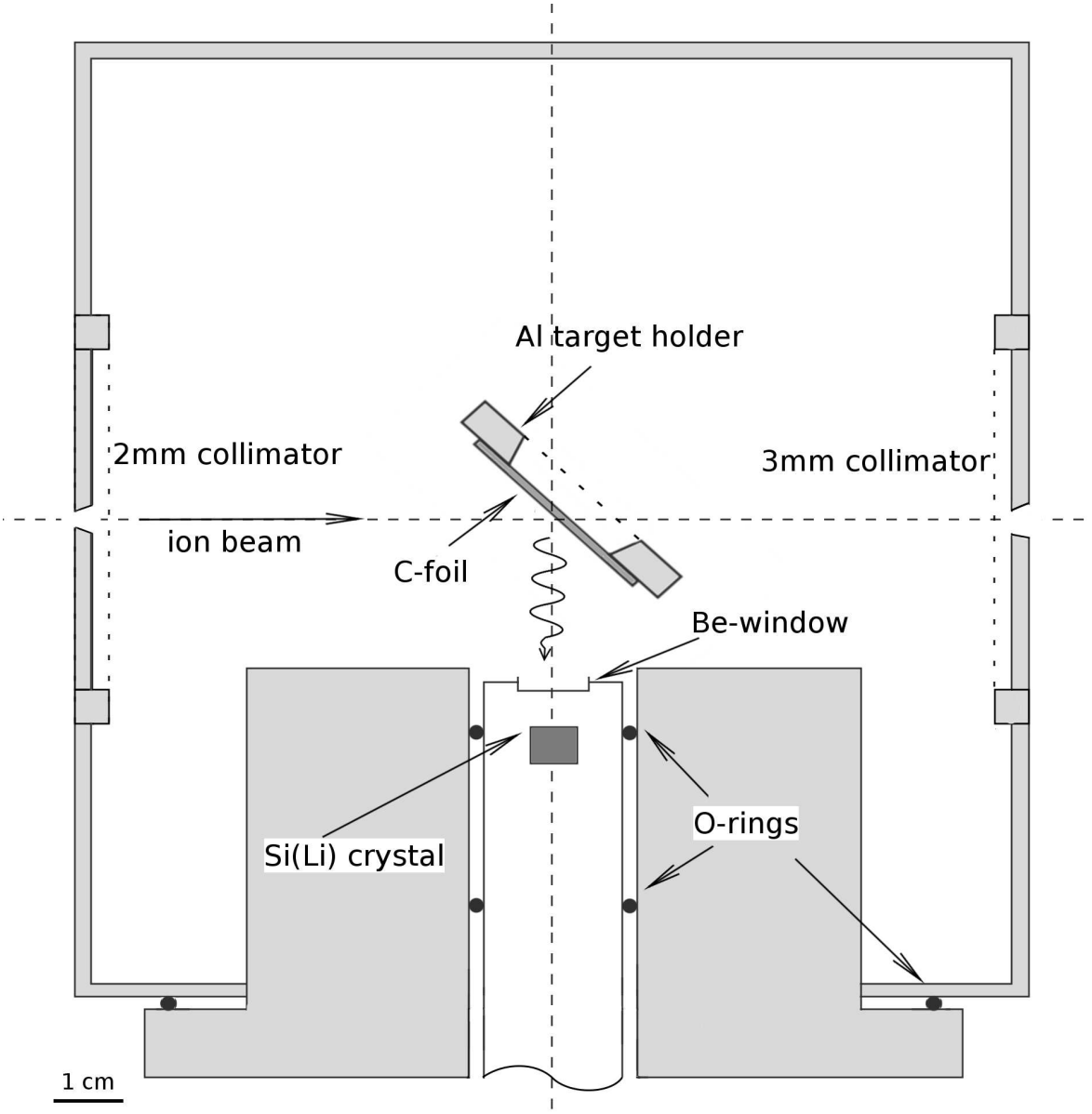


Figure 4.4: The experimental target chamber in 1:1 scale.

The target chamber was designed in a way that minimizes the distance between detector window and target center. The total crystal-target distance achieved was about 25 mm, which gives a detection solid angle of $\Delta\Omega = 0.044(1)$ sr.

Emitted x-rays were registered by an ORTEC single crystal Si(Li) detector placed perpendicular to the beam direction. The crystal of 6 mm diameter and 3 mm thickness, together with a 7.5 μm Be-window, gave a detection efficiency in the energy range 2-4 keV better than

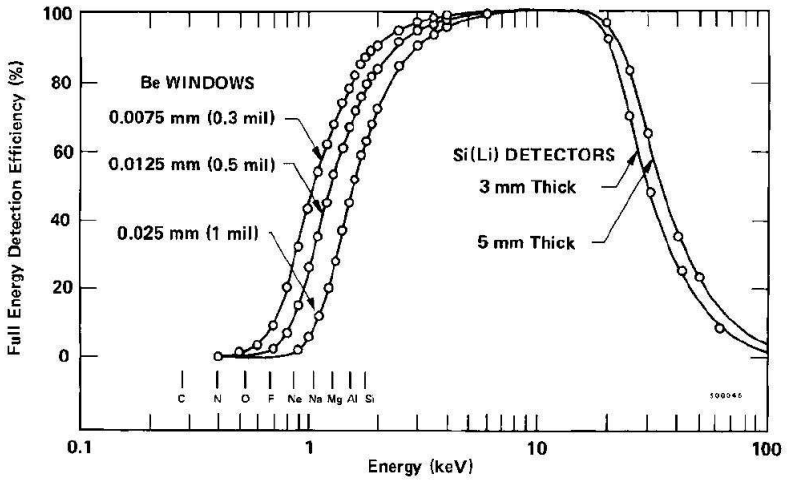


Figure 4.5: Detection efficiency of ORTEC Si(Li) detectors [ORTa].

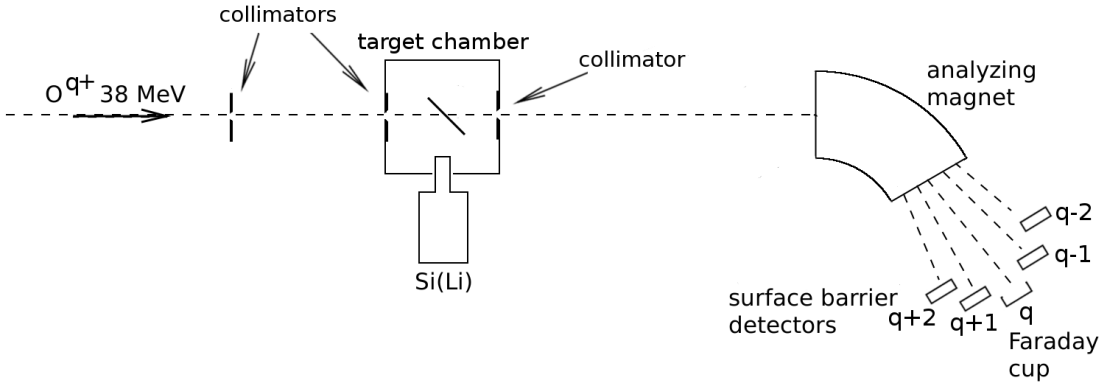


Figure 4.6: Experimental setup.

90% (Fig. 4.5). The detector was energy calibrated with a standard ^{55}Fe calibration source. Calibration was frequently repeated throughout the experiment in order to check the stability of the data acquisition system.

Along the beam direction, a set of two collimators was placed in front of the target chamber. The distance between collimators was about 2 m. Collimator apertures of 2 and 3 mm were to ensure a good beam collimation. An additional collimator between the target and magnet prevented scattered ions from entering the spectrometer and generating false coincidences (see Fig. 4.6).

The target chamber was followed by a magnetic spectrometer. The magnetic field of the dipole magnet separated the final charge states of the ions and directed them towards four surface barrier detectors. The primary beam was registered by a Faraday cup. Surface barrier detectors counted ions with charge states equal to $q-2$, $q-1$, $q+1$ and $q+2$, where q is the charge state of the primary beam. Both the magnetic field of the spectrometer and the position of the surface barrier detectors were adjustable and created a versatile system, which could be used for various beam charge states and energies. A schematic drawing of the experimental setup is presented in Fig. 4.6.

4.3 Data acquisition system

The data acquisition system was designed for registration of x-rays as well as particles with final charge states of $q-2$, $q-1$, $q+1$ and $q+2$ in a way that allowed for a software analysis of photon-particle coincidences. A schematic drawing of the electronics is presented in Fig. 4.8. For the clearness of presentation only a setup for one particle detector is drawn.

Signals from the particle detectors were first amplified by ORTEC 474 timing filter amplifiers (TFA), converted to a logic signal by constant fraction discriminators (ORTEC 463 or 473) and finally used as the STOP signals for time to amplitude converters (TAC, ORTEC 566).

A signal from the x-ray detector preamplifier was amplified and split (into two unipolar and one bipolar signals) by the Tennelec 244 spectroscopy amplifier. Additionally, a signal from the backside input of the amplifier was used (it is an unchanged signal from the front input) as an input for the TFA (ORTEC 474). The unipolar signals were processed by linear gate stretchers (LGS, ORTEC 542), while the bipolar signal was analyzed by a timing single channel analyzer and then converted to a logic signal by the delay generator (Phillips Sci 794), so that it could be used as a strobe signal for TAC, LGS modules and the ADC. The same signal was also used as a master trigger for the computer. Additionally, the TFA signal was used as a gate for one of the LGSs. This resulted in registration of only x rays which gave the START signal for the TAC. The 'non-gated' LGS served as a check of the x rays lost by the TFA. It was seen from the data that about 25% of the x-rays were not accepted by the TFA.

In Fig. 4.8 a signal from the 'gated' LGS is called 'fast', while the one from the 'non-gated' LGS is referred to as 'slow'. The x-ray timing signal was used as a START signal for TACs.

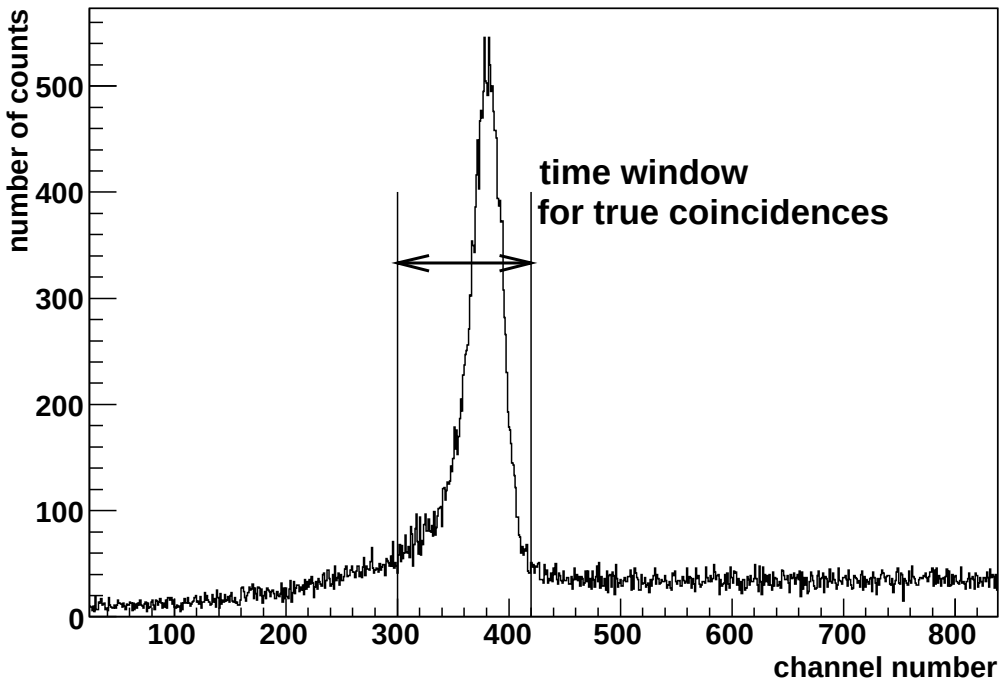


Figure 4.7: Example of a time spectrum registered during the experiment. The arrow indicates the width of a time window for true coincidences (calibration 2 ns/channel).

All the TAC and LGS outputs were registered by the ORTEC 811 ADC and the data were written into SpecTCL `.evt` list mode files and converted afterward into `.ROOT` files for analysis purposes. The CERN-ROOT software was used for data analysis.

The construction of the data acquisition system allowed for registration of the time difference between photon and particle detection with a resolution of 86(4) ns (FWHM of the time peak, Fig. 4.7). This information was used for determination of the true coincidences between registered photons and ions. An example of a time spectrum registered during the experiment is presented in Fig. 4.7. The peak associated with true coincidences is clearly visible and the time window set for data analysis is marked with an arrow. The remaining parts of the time spectrum include random coincidences that were, after normalisation, subtracted from the coincidence spectrum.

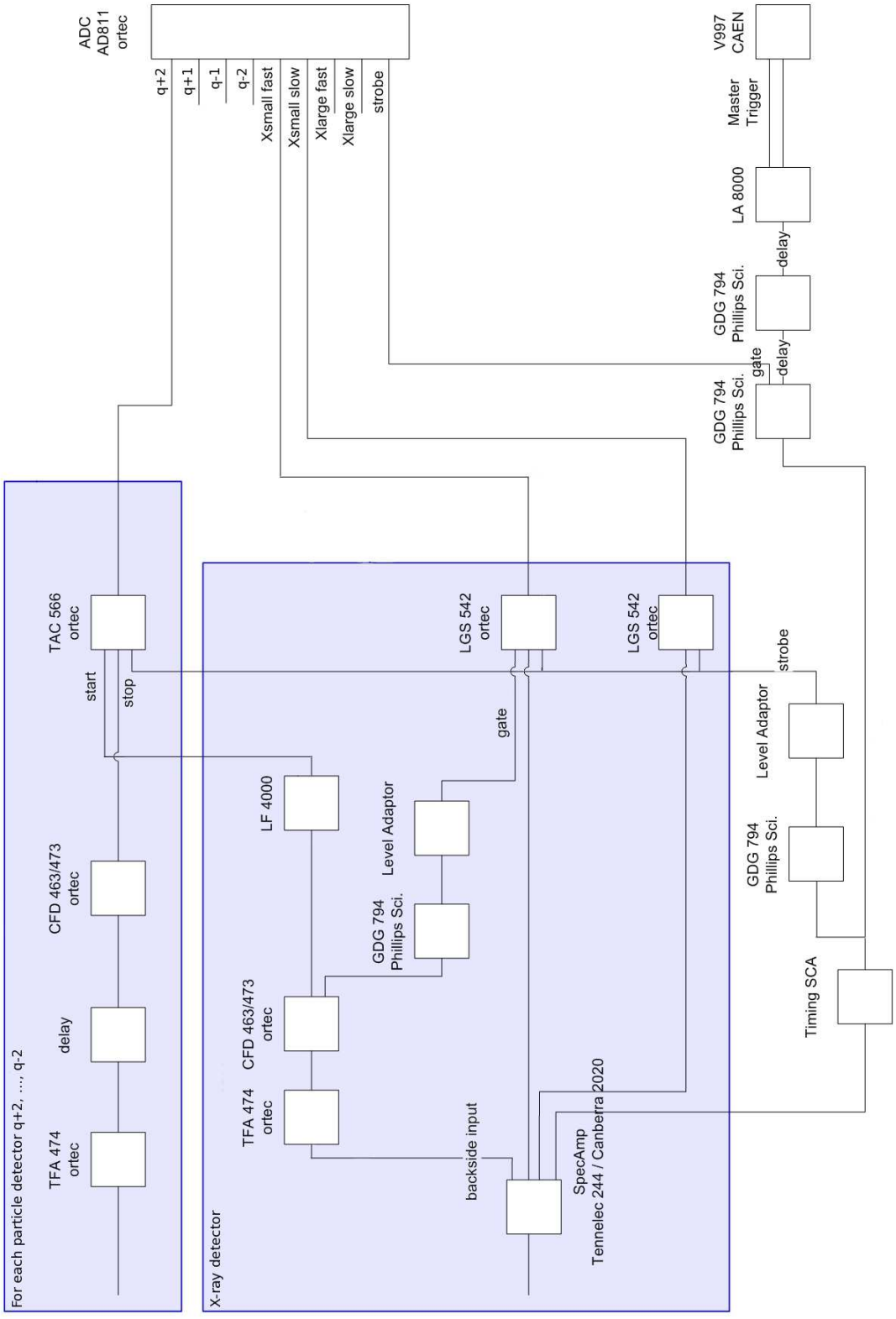


Figure 4.8: Scheme of the data acquisition system.

Chapter 5

Data analysis

The main goal of the experiment was observation of the x rays generated by bare oxygen ions (O^{8+}) impinging on carbon at an energy of 38 MeV. This gives a projectile velocity of 9.7 a.u., which corresponds to the adiabacity parameter ξ_O of 0.82. As can be seen in Fig. 5.1 (a), the single x-ray spectrum registered during O^{8+} + C collisions is dominated by the Al K-α line, which is produced by scattered ions hitting the aluminum target holder. In order to establish the shape of this line a run without the carbon foil was performed. The resulting spectrum, which contains only the Al K-α line, is represented by the dashed line in Fig. 5.1 (a). In Fig. 5.1 (b) the O^{8+} + C spectrum after subtraction of the Al K-α line is shown.

A run with 38 MeV O^{7+} ions was made to check if the structure of the x-ray spectra in the RDEC region changes when one electron in the projectile K-shell is present. As the experiment was aimed at observation of RDEC mainly to the ground state ($1s^2$), presence of a $1s$ electron in the H-like ion should block this process. Thus, a change in the RDEC range of the x-ray spectrum should be registered. As shown in Fig. 5.1 (c), the structure in the RDEC region is different for the O^{7+} ions.

As an additional test of the experimental conditions, PIXE analysis of the target foil was performed with 2.375 MeV protons, i.e. for the same collision velocity as for O^{8+} ions. During this process the impinging proton beam excites atomic states of the atoms within the material, which then deexcite emitting characteristic x rays. Intensities of the lines allow for estimation of the amount of the impurities in the material. Here, PIXE analysis was performed to check if any impurities that might produce x rays in the RDEC range are present in the foil. As

can be seen in Fig. 5.1 (d), no structure in the RDEC region was observed, nor was there evidence for REC around the photon energy of 2 keV.

Coincidence spectra obtained for bare O^{8+} ions capturing one or two electrons are presented in Fig. 5.2. These spectra were obtained using the coincidence condition on the appropriate time spectra as described in Section 4.3. The contribution of random events was subtracted. In both spectra, a well separated structure in the RDEC region is evident. The REC counts associated with ions which captured two electrons come from multiple capture processes in the target with at least one radiative capture (REC). This could not be avoided due to a very high cross section for nonradiative electron capture, which is of the order of 0.2 Mb, as estimated according to the commonly used scaling formula [Sch 83]. Another origin of these REC counts is the DREC process, which, due to a cross section of 48 b (Eq. 2.20), is a source of about 10% of the total number of counts in the REC energy range.

The following subsections of this chapter will address the data analysis in detail.

5.1 PIXE analysis of the target material

To check if there is any statistically significant structure in the RDEC range of x-ray spectrum obtained for the proton beam, the method described in Appendix A was used. The value of α was set to 0.05, which means that the probability that any structure in the tested range of the spectrum is due to statistical fluctuations (H_0 hypothesis) is equal to 0.95. A very crucial step of this analysis was a proper estimation of the background in the vicinity of the RDEC range. As can be seen in Fig. 5.3 the background shape is not very smooth and a standard linear fit of the background, implementing the least squares method, was very sensitive to the choice of the fitting region. That is why the following method of estimation of the background parameters was used. A region on both sides of the RDEC range (marked with dashed lines in Fig. 5.3), without the Al K-α line, was integrated and the result was divided by the number of channels in the chosen range of the spectrum. This gave an average number, N_{ch}, of the background counts per channel, $N_{ch} = 6.40(23)$. This number multiplied by the number of channels in the RDEC region of the x-ray spectrum gave the total number of the background counts of $b = 895(32)$. The total number, N, of counts registered within the RDEC region of the spectrum is equal to 903(30).

Table 5.1: Results of a χ^2 test of the RDEC range of the proton induced spectrum.

N_{ch}	N	b	T	$1-\alpha_T$
6.40(23)	903(30)	895(32)	0.372	0.54

The above values of N and b determined the value of the statistical variable T (Eq. A.4) to be equal 0.372. This gives $1-\alpha_T = 0.54$, which means that the H_0 hypothesis cannot be rejected. In other words, there is no evidence for any peak structure, that could be a result of any physical process, in the RDEC range of the proton induced spectrum. Thus, it can be assumed that there are no target impurities that could emit photons in the RDEC energy range. Values of all the relevant parameters are given in Table 5.1.

5.2 Projectile K- and L-shell electron loss

It could be already noticed that the events in the RDEC range are more frequent in the spectrum associated with the single charge exchange rather than with the double charge exchange channel (Fig. 5.2). Similarly, most of the REC photons are observed in the singles spectrum and not in the single charge exchange channel (compare Figs 5.1 (b) and 5.2 (b)). It is likely that after the observed capture process the ion may lose one of the captured electrons. This is due to the fact that, even in a very thin carbon foil, the electron loss probability is very high for the weakly bound ionic systems that are formed during the collision. Electron loss cross sections obtained by interpolation of relevant data (see Chapter 2) are given in Table 5.2. These cross sections are in fair agreement with the data of Shima et al. [Shi 92], where the bare and H-like ions are indicated as the most populated charge states observed when a 38 MeV oxygen beam traverses through a carbon foil. Together, they account for more than 80% of the final charge states, with 50% in the H-like (7+) state. For the system investigated, the electron loss cross sections are at least 3 orders of magnitude greater than the REC cross section. This means that there is a very high probability for an ion, after the capture process, to undergo another collision, which is most likely to be accompanied by the electron loss process.

For the system investigated, the cross section for the removal of the L-shell electron is about an order of magnitude greater than that for the K-shell electron (see Table 5.2). Thus, in case of double capture to the $1s^1 2s^1$ state, the $2s$ electron is promptly removed, while in

Table 5.2: Electron loss cross sections for oxygen ions at 38 MeV estimated from the data presented in [Bom 89, Tan 91, Hip 87].

	Process	Cross section [Mb]
L-shell ionization	$O^{5+} \rightarrow O^{6+}$	19.0
K-shell ionization	$O^{6+} \rightarrow O^{7+}$	3.6
	$O^{7+} \rightarrow O^{8+}$	0.4
	$O^{6+} \rightarrow O^{8+}$	0.1

case of capture to $1s^2$ the final charge state of the ion is more likely to remain unchanged. Therefore, one would expect most of the photons originating from RDEC to the projectile excited state to show up in the single charge exchange channel, while the capture to the ground state will be less affected by the K-shell electron loss process. This can be observed in Fig. 5.2, where the $1s^1 2s^1$ peak is clearly visible in the $q-1$ coincidence spectrum, while it is almost absent in the $q-2$ channel, compared with the structure associated with the capture to the $1s^2$ state which is still visible in the $q-2$ channel.

The cross section for double electron loss ($O^{6+} \rightarrow O^{8+}$), even though it is much smaller than that for single electron loss, was also considered. Due to this process, in some cases, both captured electrons could be removed from the ion and the RDEC events might be observed only in the singles spectrum. However, after subtraction of all the background contributions (Al K-α, REC, bremsstrahlung) the remaining number of counts within the RDEC range of the singles spectra was consistent with the sum of all the counts from the $q-1$ and $q-2$ coincidence channels. This means that these two channels include all the registered events that could be associated with the RDEC process and the sum of the RDEC counts from both channels should be included in the cross section estimation. In case of REC, in order not to lose any of the registered events, the total number of REC photons was obtained from the singles spectra.

5.3 Background processes

For such a subtle effect as the RDEC process, estimation of the background shape in the RDEC range of the x-ray spectrum is of a great importance. The most significant processes

occurring during collisions of bare ions with solid target that can contribute to the observed x-ray spectrum, are:

- radiative electron capture to continuum (RECC),
- secondary electron bremsstrahlung (SEB),
- atomic bremsstrahlung (AB),
- nucleus-nucleus bremsstrahlung (NB),
- the high energy tail of the single REC profile caused by the momentum distribution of the target electrons (Compton profile).

Under the experimental conditions, the high energy limits for the RECC (T_r) and the SEB (T_m) processes are 1.3 keV and 5.2 keV, respectively (see Eqs 2.8 and 2.9). Therefore, RECC will not contribute to the RDEC background, as it appears in the low photon energy range. In addition, RECC will be suppressed by the absorption in the Be-window. The SEB process might be a significant background contribution and will be discussed further.

There are three bremsstrahlung contributions in the x-ray spectra within the RDEC photon energy range: SEB, AB and NB. Secondary electron bremsstrahlung and atomic bremsstrahlung can be estimated by simple scaling from the data obtained by Folkmann for protons of similar velocity to the oxygen ions used during the experiment. The x-ray spectrum for p + C collisions given in [Ish 06] can be easily transformed by means of appropriate scaling formulae (Eqs 2.10-2.12). As can be seen in Fig. 2.8, this x-ray spectrum is dominated by electron bremsstrahlung (SEB + AB) for photon energies up to 10 keV, which is far beyond the region of interest (2.8-4.2 keV). According to the formula given by Eqs 2.13-2.15, the cross section for the NB process is of the order of 1 mb/keV sr in the RDEC range, which is a few orders of magnitude smaller than the cross sections for any of the electron bremsstrahlung processes. Thus, the contribution from NB can be neglected in the discussed case.

Another contribution that should be taken into account is the high energy tail of REC. The observed REC structure originates not only from single radiative electron capture, but can also be associated with the noncorrelated double electron capture (DREC). However, estimation based on Eq. 2.20 shows that the DREC cross section is an order of magnitude smaller than that for a single REC process, as shown in Table 5.3.

Table 5.3: Total cross sections for the background processes that were taken into account during data analysis.

Process	Cross section [kb]
Radiative electron capture (REC)	0.512
Nonradiative electron capture (NREC)	240.0
Double radiative electron capture (DREC)	0.048

All these background contributions are shown in Fig. 5.4. In the expected RDEC energy region (2.8-4.2 keV) the broad REC spectrum significantly exceeds the bremsstrahlung contribution (see inset in Fig. 5.4). As a consequence, the RDEC line will be placed mainly on the REC tail.

The cross section for background contributions was also corrected for the detection efficiency of the Si(Li) detector. Both crystal efficiency and Be-window absorption were taken into account by using the data shown in Fig. 4.5. The shape of the background, after efficiency correction, is also shown in Fig. 5.4. It can be noticed that the spectrum is completely dominated by the tail of the single REC line and the contribution of the bremsstrahlung is almost negligible. Additionally, the low energy photons (energy not exceeding 0.5 keV) are completely absorbed in the beryllium window of the x-ray detector and the curve, representing the sum of all background contributions corrected for the detector efficiency, drops almost to zero at low photon energies.

5.4 Pile-up of single REC photons and its contribution to the RDEC energy range of the spectrum

As the energy of a RDEC photon is about twice as large as the energy of a single REC photon, it might be impossible to distinguish a real RDEC event from a situation when two REC photons are simultaneously registered by the x-ray detector (pile-up effect). This process may produce an additional background within the RDEC range of the x-ray spectrum. Simultaneous detection of two REC photons may occur in three situations:

- both photons emitted during the DREC process propagate in the same direction and are both registered by the x-ray detector,

Table 5.4: Probabilities and count rates of the processes that might contribute to the x-ray spectrum in the RDEC range. For more information see text.

Process	Probability	Count rate [events/s]
RDEC	$5.3{\cdot}10^{-11}$	$1.6{\cdot}10^{-6}$
DREC	$6.0{\cdot}10^{-11}$	$1.8{\cdot}10^{-6}$
double REC collisions	$5.2{\cdot}10^{-14}$	$1.6{\cdot}10^{-9}$
sequential REC	–	$2.2{\cdot}10^{-10}$

- the ion undergoes multiple collisions during which at least twice the REC process occurrs and both photons are emitted towards the x-ray detector,
- if the beam intensity is high enough, there is a chance that two REC photons emitted by two sequential ions are simultaneously detected by the x-ray detector.

If the cross section for RDEC is of the order of 0.1 b [Nef 09] and the given geometry of the experiment is taken into account, one obtains the probability of observation of a RDEC photon during an ion-atom collision equal to $5.3 \cdot 10^{-11}$. If the beam intensity is equal to $I_{medium} = 3 \cdot 10^4$ ions/s, which is the mean value obtained during the experiment, the RDEC count rate will be of about $1.6 \cdot 10^{-6}$ events/s for the geometry applied (Table 5.4).

For a low-Z system, as the one used during the experiment, the cross section for the noncorrelated double electron capture (DREC) is rather high (see Table 5.3) when compared to the RDEC cross section. Thus, simultaneous observation of both DREC photons might contribute to the count rate in the RDEC range. The probability that both DREC photons will be registered as one event is estimated to be comparable with the probability of registration of a true RDEC event (Table 5.4). As the angular correlations of these two emitted photons have so far neither been measured nor calculated, it was assumed that the angular distribution of the two DREC photons is the same as for the REC photons ($\sim \sin^2\theta$) and the emission angles for the photons are independent of each other. This assumption may cause a significant overestimation of the corresponding probability given in Table 5.4. It is more likely that the photons are emitted in opposite directions (momentum conservation) and the corresponding count rate is much lower than estimated above.

For an REC cross section of 512 b the probability that one ion undergoes two collisions in the target, with the REC process occurring in each of them, and that both photons are registered as one event, is about $5.2 \cdot 10^{-14}$. This, together with the mean beam current value,

results in a count rate of double REC photons as a single event on the order of 10^{-9} events/s, which is negligible when compared to the expected count rate of the RDEC photons (Table 5.4).

Another possibility of simultaneous detection of two REC photons is the observation from two incoming ions successively undergoing REC processes in the target. This random event may be registered only in the time window of the order of the charge collection time in the silicon detector. For a typical Si(Li) crystal the collection time does not exceed 100 ns [Lip 00]. In case of an ORTEC silicon detector cooled with LN_2 it is on the order of 10 ns [ORTb]. Therefore, the corresponding count rate for the mean beam intensity value is on the order of 10^{-10} events/s and can be neglected. This estimation can be tested by the analysis of the N_{RDEC}/N_{REC} ratio as a function of beam intensity I. The count rate of this random event scales with I^2, while all the other count rates (Table 5.4), including that for single REC, scale with I. Thus, if only true (RDEC) events are registered, the number of counts in both REC and RDEC regions will be proportional to the beam intensity and the ratio N_{RDEC}/N_{REC} should be independent of I. If a pile-up effect, due to sequential REC collisions was observed in the RDEC region, N_{RDEC} would be proportional to the square of the beam intensity and the N_{RDEC}/N_{REC} ratio would increase with the beam intensity. In order to separate the data collected with different beam intensities registered during data taking, data files were sorted according to the average beam intensity and separated into three groups:

- data taken with average beam current not exceeding $2.5 \cdot 10^4$ ions/s (average of all files: $I_{low} = 2.0 \cdot 10^4$ ions/s) – further referred to as low intensity beam;
- data taken with average beam current greater than $4.0 \cdot 10^4$ ions/s (average of all files: $I_{high} = 4.3 \cdot 10^4$ ions/s) – further referred to as high intensity beam;
- all the remaining data (average beam intensity: $I_{medium} = 3.0 \cdot 10^4$ ions/s).

This gives a beam intensity ratio $I_{high}/I_{low} = 2.15$, which, if the pile-up effect was observed in the RDEC region, would increase the RDEC to REC ratio by a factor of almost 5.

For the discussed beam intensities the N_{RDEC}/N_{REC} ratio is shown in Fig. 5.5 for the $q-1$ coincidence channel. It can be seen in this figure that the ratio does not change within the uncertainty limits, which means that no pile-up events were registered in the RDEC region. These results do not exclude the contribution of the DREC process. However, the upper limit of this contribution is known and will be used in Chapter 7 for further discussion.

Table 5.5: Calculated positions of the RDEC and REC peaks in the x-ray spectrum corresponding to different combinations of the initial and final states of the captured electrons. All values are given in keV.

Process	Captured target electrons		
	Valence	One K-shell and one valence	K-shell
REC	2.16	–	1.88
RDEC $1s^2$	4.18	3.91	3.64
RDEC $1s^1 2s^1$	3.58	3.31	3.04

5.5 Single spectra analysis

In order to eliminate the Al K-α line from the O^{8+} + C data, single spectra obtained for bare ions without the carbon target were normalized and subtracted from the data taken with the foil. As the shape of the Al K-α line, despite a good statistics, was not smooth enough, the line in the spectrum taken without the target foil could not be normalized to the one in the O^{8+} + C spectrum by simple comparison of the maxima of the lines. To establish the peak height of the Al K-α line in both spectra, the numbers of counts around the centroid of the Al K-α line in each x-ray spectrum were integrated and divided by the number of channels in the region of integration. This procedure prevented the contribution of the Al K-α line from being overestimated. Al K-α line normalized to the spectrum taken with the foil is shown in Fig. 5.6.

After subtraction of the Al K-α line, the REC structure in the single spectrum was clearly resolved, as shown in Fig. 5.7. For the investigated low energy collisions the binding energy of the target electron cannot be neglected, as it can significantly contribute to the REC photon energy (see Eq. 2.2). For the considered collision system the captured electron could come either from the target K-shell or from the target valence band. Thus, a double peak structure in the REC region was expected, with the peaks separated in the spectrum by the difference in the binding energy of the K-shell and valence electrons in the carbon foil, which is about 280 eV [Tho 01]. Expected positions of the corresponding REC peaks are given in Table 5.5. As can be seen in Fig. 5.7, the obtained x-ray spectrum is well described by the sum of the target K-shell and valence band Compton profiles.

Table 5.6: Results of a χ^2 test of the RDEC range of the coincidence spectra.

	N	b	T	$1-\alpha_T$	N_{RDEC}	β
$q-1$	567(23)	241(13)	25000	<0.0001	326(27)	<0.0001
$q-2$	31(6)	0.035(3)	420	<0.0001	31(6)	<0.0001

The total number N_{REC} of the REC photons collected during the experiment was N_{REC} = 39800(200). The uncertainty includes both the statistical error and the uncertainty generated during the subtraction of the background contribution.

5.6 Coincidence spectra analysis

In order to establish the significance of the observed structure within the RDEC energy range of the coincidence spectra (Fig. 5.2) the method described in Appendix A was applied. The first step was to check whether the observed structure was due to statistical fluctuations (H_0 hypothesis). Similar to the PIXE analysis, $\alpha = 0.05$ was assumed. Then, the background contribution in each spectrum was obtained by integration of the REC Compton profile fit over the RDEC energy range (2.8-4.2 keV). This gave the total number of the background counts in the $q-1$ and $q-2$ spectra of $b^{q-1} = 241(13)$ and $b^{q-2} = 0.035(3)$. The total number of counts accumulated in the RDEC energy range during the experiment was N^{q-1} = 567(23) and $N^{q-2} = 31(6)$ for the single and double charge exchange channels, respectively. These gave the value of the statistical variable (Eq. A.4) of $T^{q-1} \approx 25000$ and $T^{q-2} \approx 420$, which corresponds to the value of $\alpha_T > 0.9999$ for both $q-1$ and $q-2$ channels. Thus, in both cases the hypothesis H_0 has to be rejected, as the probability that the observed structure is due to statistical fluctuations is less than 0.0001. This means that the observed structure is a result of a physical process (H_1 hypothesis) and the number of counts associated with this process is: $N^{q-i}_{RDEC} = N^{q-i} - b^{q-i}$, where $i = 1, 2$, with the uncertainty given by $\Delta N^{q-i}_{RDEC} = \sqrt{(\Delta N^{q-i})^2 + (\Delta b^{q-i})^2}$. This leads to numbers of the RDEC counts of $N^{q-1}_{RDEC} = 326(27)$ and $N^{q-2}_{RDEC} = 31(6)$ for the single and double charge exchange channels, respectively. Additionally, as given in Eq. A.16, the type two error (β) can be estimated. In the case discussed here, the value of β is less than 0.0001 which is beyond the statistical significance. Values of all the parameters for both single and double charge exchange channels are given in Table 5.6.

Subtraction of the Compton profile based on Ref. [Big 75] from the coincidence spectra (Fig. 5.2) revealed a complex structure of the RDEC line. The resulting spectra are presented in Figs 5.8 (c) and (d). The observed structure comprises at least two maxima which can be assigned to the RDEC process. It is not only a result of capture to the ground ($1s^2$) and excited ($1s^12s^1$) states of the projectile (see Fig. 5.8 (b)), but can also be attributed to the capture of either K-shell or valence target electrons. Combinations of the initial and final electron states accessible for the process and the resulting RDEC peaks positions are given in Table 5.5. The possible transitions are shown in Fig. 5.8 (a) with the positions of the lines representing their contributions to the RDEC x-ray spectrum (Fig. 5.8 (b)). For this presentation, probabilities of all the possible RDEC transitions were assumed to be equal. This spectrum should be compared with the data obtained experimentally in the single and double charge exchange channels after background subtraction, shown in Figs 5.8 (c) and (d). The latter fgure suggests that the transitions from the target valence band to the projectile K-shell are negligible.

In order to make at least an estimate of the contributions of all the possible transitions, the sum of lines representing all the possible processes was fitted to the sum of the x-ray spectra registered in the $q-1$ and $q-2$ coincidence channels. The result is presented in Fig. 5.9 and the fitting parameters are given in Table 5.7. It can be noticed that in case of transitions which included at least one target valence electron the corresponding areas below the fitted curve are close to zero. Based on this observation, it can be deduced that the transitions from the valence band to the $1s^12s^1$ state, which overlap with the K-shell $\rightarrow 1s^2$ transition, are also negligible.

Thus, transitions from the valence band were practically not present in the RDEC spectrum. Moreover, the ratio, R_A, of the areas under the curves representing transitions from the target K-shell to the excited and ground projectile states, $R_A = A_{1s^12s^2}/A_{1s^2}$, is equal to 0.500(68) This value reflects the ratio of the RDEC cross sections for capture to the excited and ground states $\sigma^{1s^12s^2}_{RDEC}/\sigma^{1s^2}_{RDEC}$. The theoretical value of this ratio can be estimated from Fig. 3.5 for the adiabacity parameter of $\xi_O = 0.82$, which corresponds to the experimental conditions. The theoretical value of this cross section ratio is equal 0.7, which is close to the experimental result.

Table 5.7: Areas (A) of the shapes of the RDEC contributions fitted to the sum of $q-1$ and $q-2$ spectra. The FWHM of all lines was set to 0.3 keV which is the width of the carbon Compton profile.

Transition	Peak position [keV]	Area (A)
$2 \times$ K-shell $\rightarrow 1s^1 2s^1$	3.04	118(11)
$1 \times$ K-shell $+ 1 \times$ valence $\rightarrow 1s^1 2s^1$	3.31	0.0(1.9)
$2 \times$ valence $\rightarrow 1s^1 2s^1$ or $2 \times$ K-shell $\rightarrow 1s^2$	3.62	237(11)
$1 \times$ K-shell $+ 1 \times$ valence $\rightarrow 1s^2$	3.91	0.0(2.5)
$2 \times$ valence $\rightarrow 1s^2$	4.18	2.5(9.9)

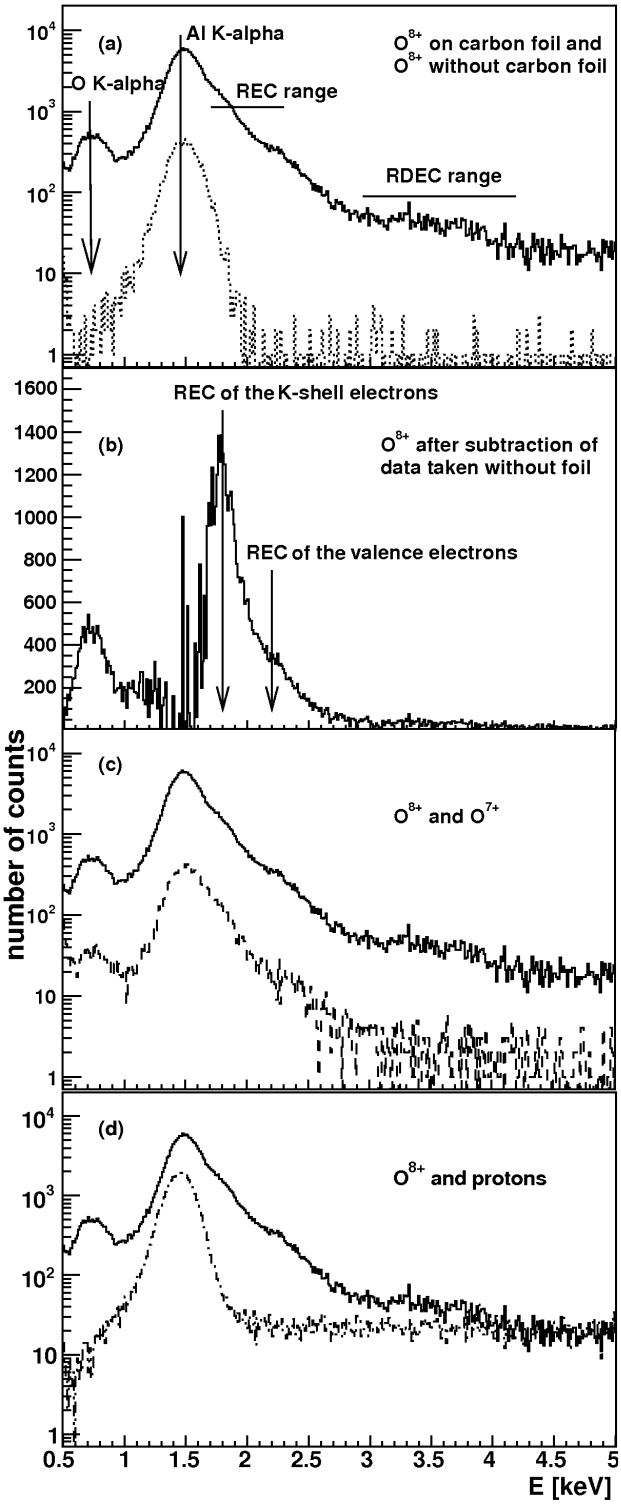


Figure 5.1: Experimental single x-ray spectra. In all spectra: solid line – 38 MeV O^{8+} + C. (a) dashed line – O^{8+} data taken without the carbon foil, (b) O^{8+} data after subtraction of the Al K-α line, (c) dotted line – 38 MeV O^{7+} + C, (d) dot-dashed line – 2.375 MeV protons on carbon.

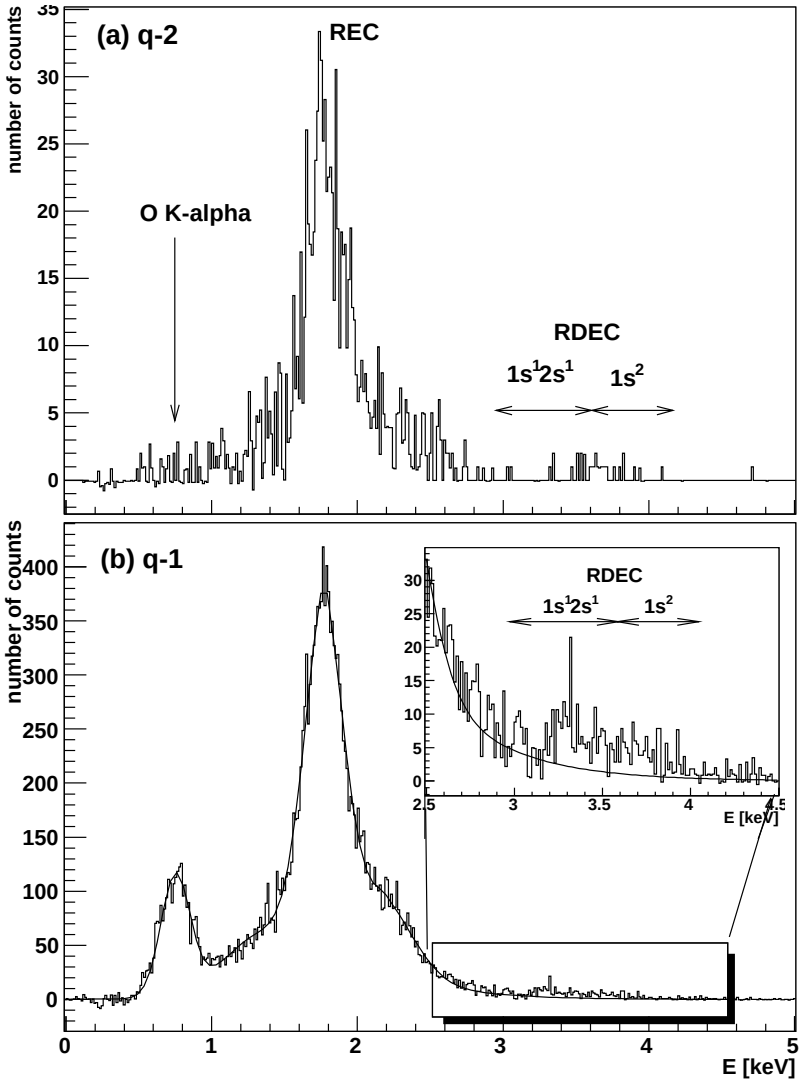


Figure 5.2: X rays registered for O^{8+} + C collisions in coincidence with ions which captured (a) two electrons and (b) one electron. Solid line is the sum of the REC Compton profile and the Gaussian shape of the oxygen K-α line fitted to the spectrum.

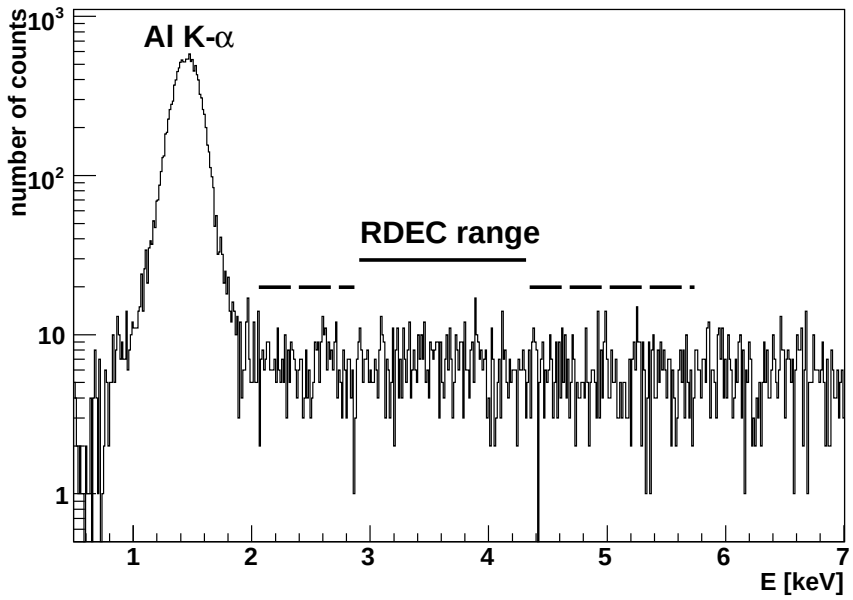


Figure 5.3: Proton induced x-ray spectrum. Solid line: the RDEC range; dashed line: region considered during background estimation.

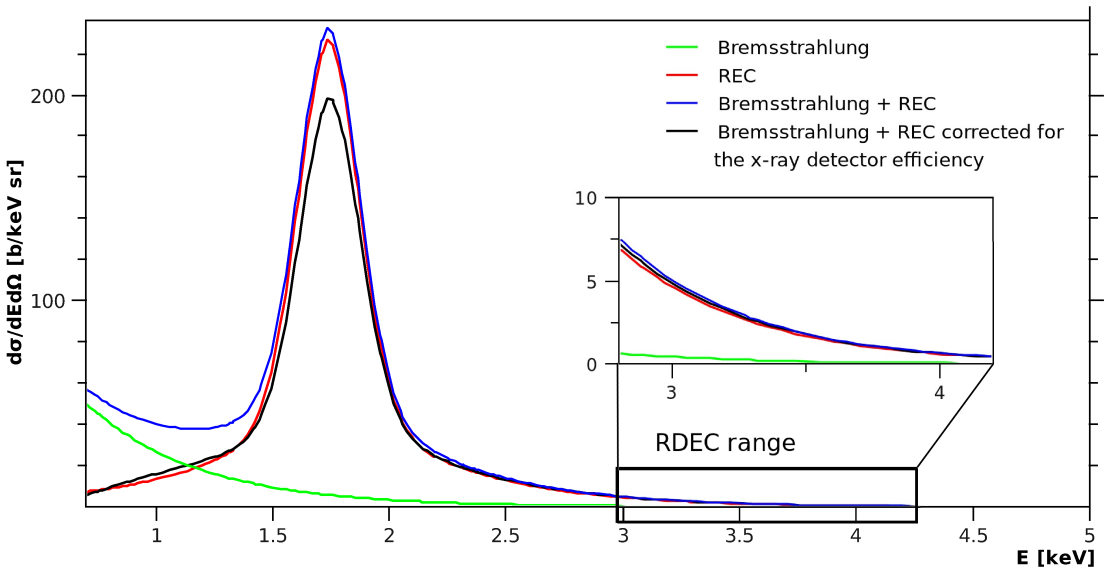


Figure 5.4: Background structure in the single x-ray spectrum. The bremsstrahlung contribution includes all the relevant processes (SEB + AB + NB) discussed in the text. The spectrum is completely dominated by the REC structure.

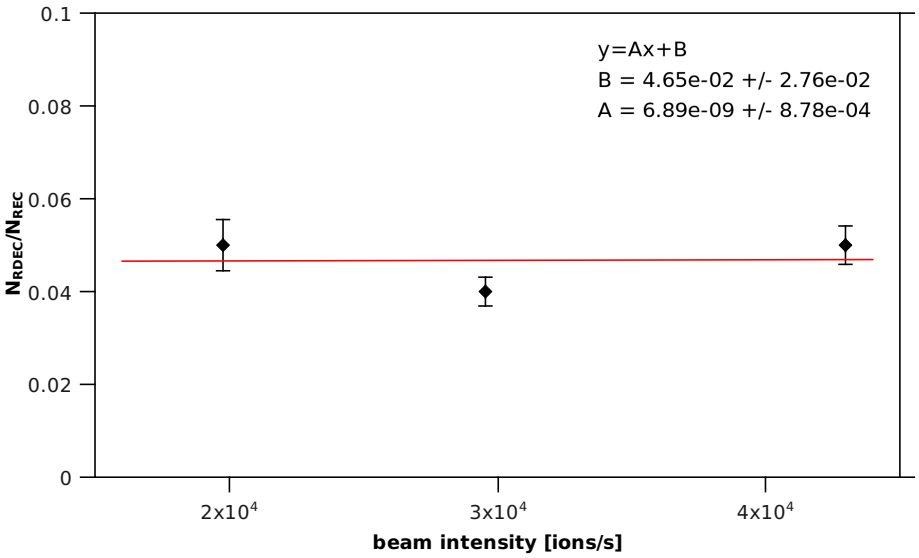


Figure 5.5: N_{RDEC}/N_{REC} ratio in the $q-1$ coincidence spectra as a function of beam intensity.

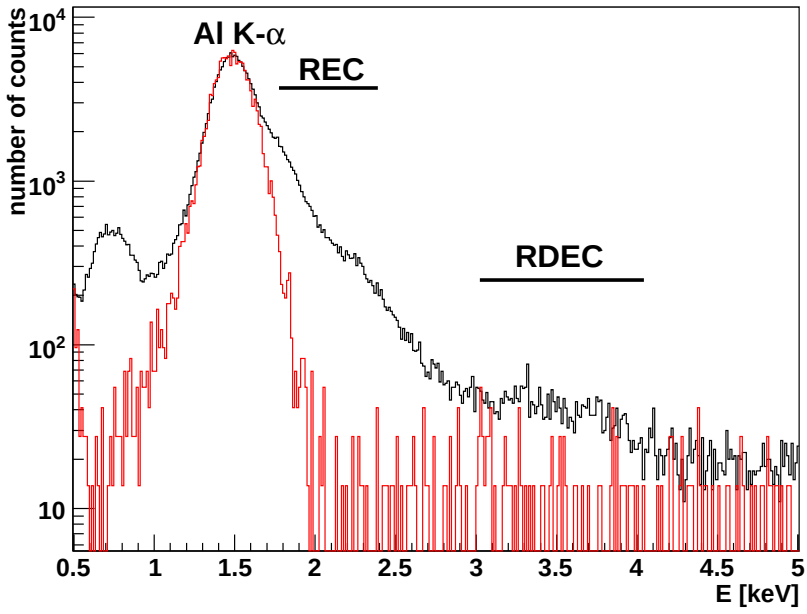


Figure 5.6: O^{8+} spectrum taken without the carbon foil (red line) normalized to the data taken with the foil (black line).

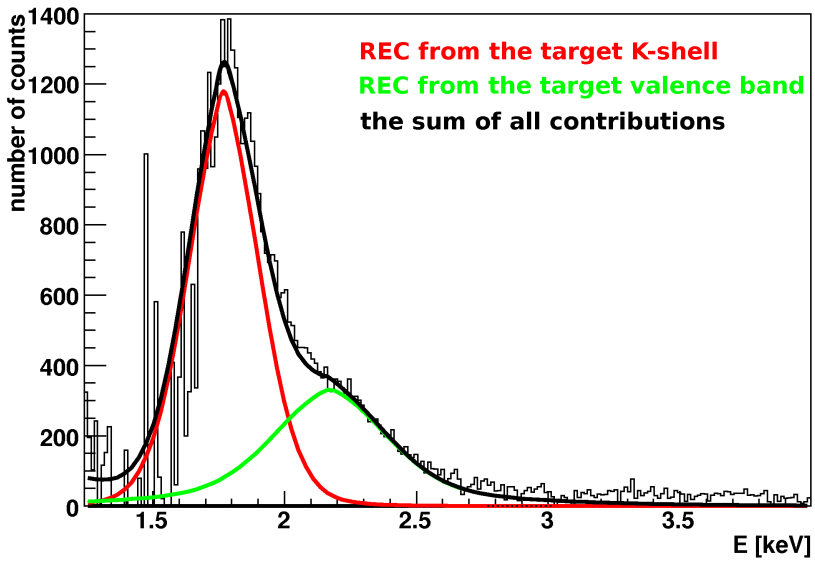


Figure 5.7: Double structure of the REC line resolved after subtraction of the Al K-α line.

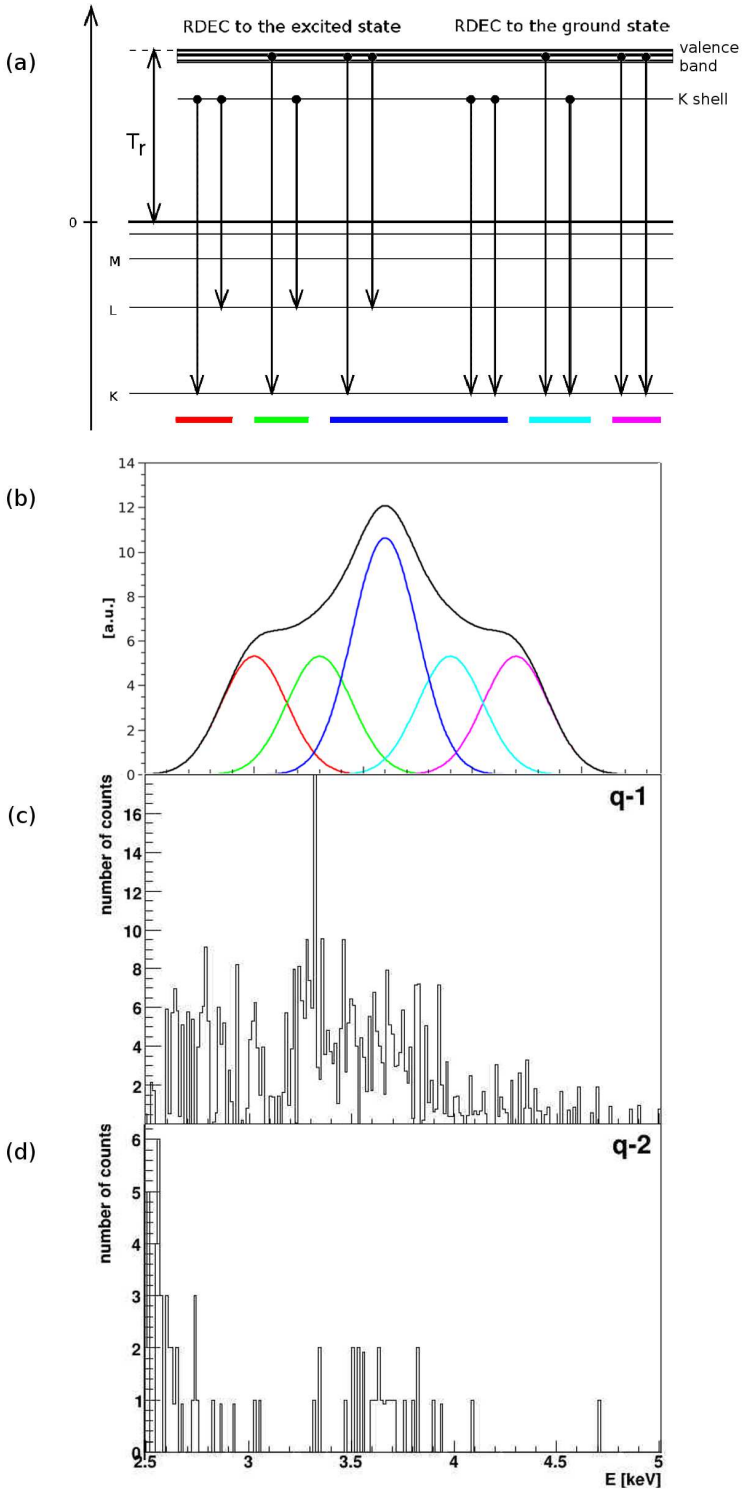


Figure 5.8: Possible RDEC transitions (a) and the structure of the produced x-ray spectrum (b) when equal cross sections for all the partial processes are assumed. Black line – the sum of all contributions. Additionally, corresponding RDEC spectra obtained experimentally in single (c) and double (d) charge exchange channels are presented.

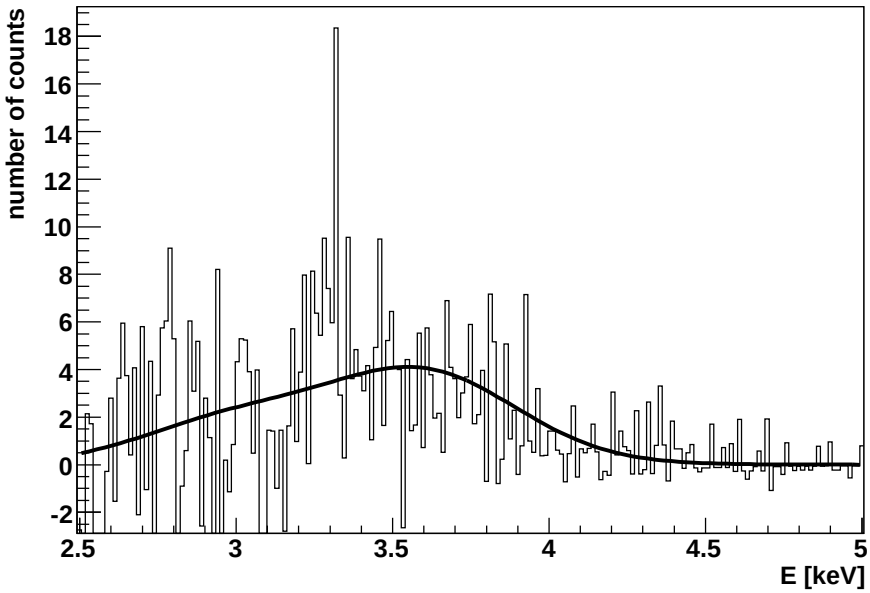


Figure 5.9: The sum of spectra registered in single and double charge exchange channels with a fit of all possible combinations of the RDEC transitions. Fitting parameters are given in Table 5.7.

Chapter 6

The RDEC cross section

6.1 Experimental value of the RDEC cross section

As it was discussed in Section 5.6, RDEC photons appeared both in single and double charge exchange channels. The numbers of counts in the coincidence spectra, $N^{q-1}_{RDEC} = 326(27)$ and $N^{q-2}_{RDEC} = 31(6)$, in single and double charge exchange channel, respectively, gave the total number of RDEC counts $N_{RDEC} = 357(28)$. The total number of the REC counts collected during the experiment in the single x-ray spectrum was $N_{REC} = 39800(200)$. The ratio N_{RDEC}/N_{REC} of the total RDEC to REC numbers of counts obtained during the experiment was equal to 0.0092(6). One can assume that:

$$\frac{N_{RDEC}}{N_{REC}} = \frac{\frac{d\sigma_{RDEC}}{d\Omega}\Big|_{\theta=90^\circ}}{\frac{d\sigma_{REC}}{d\Omega}\Big|_{\theta=90^\circ}}, \tag{6.1}$$

which, for the angular differential cross section for the REC process obtained from Eq. 2.6, gives $(d\sigma_{RDEC}/d\Omega)|_{\theta=90^\circ} = 0.71(5)$ b/sr. When the angular distribution of the RDEC photons is assumed to be the same as for the REC photons ($\sim \sin^2\theta$), one obtains the total RDEC cross section value $\sigma_{RDEC} = 5.9(4)$ b.

The registered REC photons can be emitted not only during the REC process but can also originate from the DREC process. Thus, the probability P_{REC} of observation of a single REC photon is given by:

$$P_{REC} = \left(\frac{d\sigma_{REC}}{d\Omega}\Big|_{\theta=90^\circ} + 2\frac{d\sigma_{DREC}}{d\Omega}\Big|_{\theta=90^\circ} \right) \Delta\Omega d, \tag{6.2}$$

where d is the target thickness. In case of the DREC process the cross section has to be multiplied by two, as either of the two emitted photons can be registered by the x-ray detector.

Similarly, there is a certain probability that both REC photons emitted during theDREC process are registered as a single event (see discussion of this problem in Section 5.4). Then, the probability P_{RDEC} of registration of a photon in the RDEC energy range can be expressed as:

$$P_{RDEC} = \left(\frac{d\sigma_{RDEC}}{d\Omega}\Big|_{\theta=90^\circ} + \frac{d^2\sigma_{DREC}}{d\Omega_1 d\Omega_2}\Big|_{\theta_1,\theta_2=90^\circ} \Delta\Omega \right) \Delta\Omega d, \tag{6.3}$$

where the indices 1 and 2 indicate each of the emitted DREC photons. In this case:

$$\frac{N_{RDEC}}{N_{REC}} = \frac{P_{RDEC}}{P_{REC}} \tag{6.4}$$

and the RDEC differential cross section is estimated to be $(d\sigma_{RDEC}/d\Omega)|_{\theta=90^\circ} = 0.66(39)$ b/sr. When the angular distribution of the RDEC photons is again assumed to be the same as for REC photons ($\sim \sin^2\theta$), the total RDEC cross section is equal to $\sigma_{RDEC} = 5.5(3.2)$ b. The uncertainty comes mainly from the uncertainty of the target thickness given by the maker of the foil [ACF 09]. Both the obtained σ_{RDEC} values are comparable and both are significantly greater than the total cross section based on the theoretical expectations ($\sigma_{RDEC} = 0.15$ b [Nef 09]).

When, according to the observations described in Section 5.6, the contribution of the transitions from the target K-shell to the projectile excited state are taken into account, the cross section for RDEC to the ground state, $\sigma^{1s^2}_{RDEC}$, and for the capture to the excited state, $\sigma^{1s^12s^1}_{RDEC}$, can be calculated from:

$$\begin{cases} \dfrac{\sigma^{1s^12s^1}_{RDEC}}{\sigma^{1s^2}_{RDEC}} = 0.7, \\ \sigma^{1s^12s^1}_{RDEC} + \sigma^{1s^2}_{RDEC} = \sigma_{RDEC}, \end{cases} \tag{6.5}$$

which finally leads to the values of the RDEC cross sections $\sigma^{1s^2}_{RDEC}$ and $\sigma^{1s^12s^1}_{RDEC}$ of 3.2(1.9) b and 2.3(1.3) b, for the capture to the ground and excited states, respectively. The $\sigma^{1s^2}_{RDEC}$ value is still a factor of 25 greater than the theoretical one. This leads to the ratio, R_{exp}, of the RDEC to REC cross sections of $R_{exp} = \sigma^{1s^2}_{RDEC}/\sigma_{REC} = 7.4(3.7) \cdot 10^{-3}$ which is much greater than the theoretical value based on Nefiodov calculations [Nef 09] and the Stobbe formula for the REC cross section, $R_{Nef} = 2.9 \cdot 10^{-4}$.

6.2 Estimation of the $\sigma_{RDEC}/\sigma_{REC}$ ratio in the nonrelativistic approach

Simple calculations based on the principle of detailed balance can be used to estimate the cross sections ratio $R_{nrel} = \sigma^{1s^2}_{RDEC}/\sigma_{REC}$. Eq. 3.5 expresses this ratio by means of single and double photoionization cross sections. For a given projectile atomic number Z, the ratio σ_{DPI}/σ_{PI} is almost constant and, for nonrelativistic photon energies, can be expressed as [Amu 75]:

$$\frac{\sigma_{DPI}}{\sigma_{PI}} \approx \frac{0.0932}{Z^2}. \tag{6.6}$$

As the photoionization cross section scales with the photon energy [Fan 59]:

$$\sigma_{PI} \sim \left(\frac{1}{\hbar\omega}\right)^5, \tag{6.7}$$

the ratio $\sigma_{PI}(2\hbar\omega)/\sigma_{PI}(\hbar\omega) = 1/32$ and the cross sections ratio can be written as:

$$R_{nrel} = \frac{\sigma^{1s^2}_{RDEC}}{\sigma_{REC}} = 0.00291F\frac{Z_t - 1}{Z^2}. \tag{6.8}$$

In case of the discussed experiment $Z_t = 6$, $Z = 8$ and the above formula gives, for $F = 1$, $R_{nrel} = 2.3 \cdot 10^{-4}$, which is close to the value obtained by Nefiodov. This suggests that the R_{Nef} value calculated by Nefiodov is not very far from the nonrelativistic estimation of the RDEC cross section based on the cross section for double photoionization and the principle of detailed balance.

6.3 RDEC cross section based on the Yakhontov approach

In two papers [Yak 96, Yak 97] Yakhontov calculated the value of the $\sigma^{1s^2}_{RDEC}/\sigma_{REC}$ ratio for the 11.4 MeV/u Ar^{18+} + C collisions. For a given value of the adiabacity parameter ξ, the value of this ratio scales with the projectile atomic number as Z^{-5}. In case of the argon and oxygen experiments, the value of the adiabacity parameter was comparable ($\xi_{Ar} = 0.85$ and $\xi_O = 0.82$). Thus, it was possible to use this scaling for estimation of the value of R_{Yakh} for the oxygen experiment from the value calculated by Yakhontov for the argon experiment (R^{Ar}_{Yakh}). Since for these experiments:

$$\frac{R_{Yakh}}{R^{Ar}_{Yakh}} = \frac{Z_O^{-5}}{Z_{Ar}^{-5}} = 57.66, \tag{6.9}$$

Table 6.1: Comparison of the experimental values of the RDEC cross section and the $R = \sigma^{1s^2}_{RDEC}/\sigma_{REC}$ ratio with the ones obtained from various theoretical approaches .

	Experiment	Nefiodov calculations	Non-relativistic approach	Yakhontov calculations
$\sigma^{1s^2}_{RDEC}$ [b]	3.2(1.9)	0.15	0.14	0.14
$R = \sigma^{1s^2}_{RDEC}/\sigma_{REC}$	$7.4(3.7)\cdot10^{-3}$	$2.9\cdot10^{-4}$	$2.3\cdot10^{-4}$	$2.1\cdot10^{-4}$

one obtains the value of the RDEC to REC cross section ratio for oxygen of $R_{Yakh} = 2.1\cdot10^{-4}$ which is consistent with both nonrelativistic estimations, i.e. Nefiodov calculations and the estimation based on the principle of detailed balance.

The estimations of the RDEC cross section and the $\sigma^{1s^2}_{RDEC}/\sigma_{REC}$ ratio presented in this chapter suggest that the experimentally obtained value of the RDEC cross section is much greater than theoretical estimations. Consequently, the value of the $\sigma^{1s^2}_{RDEC}$ cross section is much greater than the theoretical ones, estimated from the $R = \sigma^{1s^2}_{RDEC}/\sigma_{REC}$ ratio, as summarised in Table 6.1. However, according to Nefiodov [Nef 09], the system chosen for the experiment does not fully meet the theoretical assumptions. Since $Z \sim Z_T$, captured electrons cannot be treated as quasifree and theoretical calculations given in [Mik 04a, Mik 04b, Nef 05] might provide an underestimated cross section value. As the same assumptions for the captured electrons are applied for the other theoretical approaches to the RDEC cross section that are given in this chapter, these calculations may also give underestimated values of the RDEC cross section.

Chapter 7

Monte Carlo simulations of the x-ray spectra

It was shown in Section 6.1 that the experimental value of the RDEC cross section is significantly greater than the one predicted by Nefiodov [Nef 09]. Thus, a Monte Carlo simulation was performed in order to check the structure of the x-ray spectrum that could be obtained, assuming the value of the RDEC cross section predicted by Nefiodov was correct.

A C++ code written by Świat [Swi 99] was used. This is a simulation of x-ray spectra observed during ion-atom collisions. The x-ray spectra that can be simulated are due to radiative processes such as REC, DREC and RDEC as well as characteristic x-ray radiation. This code was thoroughly tested by its author for many collision systems [Swi 00] and was accepted as a reliable tool for simulations of x-ray spectra resulting from atomic collision processes. The simulation can reproduce almost any experimental conditions regarding beam, target and detector properties. It allows for implementation of any geometry of the x-ray detector. The parameters that have to be given in the input file are: beam diameter, target thickness, detector distance from the target center, observation angle with respect to the beam direction, detector shape and dimensions. Detection efficiency is provided as a list of data points which are interpolated for the given photon energy. A detailed description of the input parameters can be found in [Swi 00]. Here, the detector parameters were provided according to information presented in Chapter 4 and the detection efficiency was based on data given by ORTEC [ORTa] (see Fig. 4.5). The code was originally designed to reproduce the conditions of gas-jet target experiments. Thus, by default, a Gaussian distribution of gas particles was used to describe the target density. Here, the code was adopted to the experimental conditions discussed in this thesis, a thin solid target positioned at 45° to the beam direction. The coordinate system used for simulation is shown in Fig. 7.1 for $x = 0$.

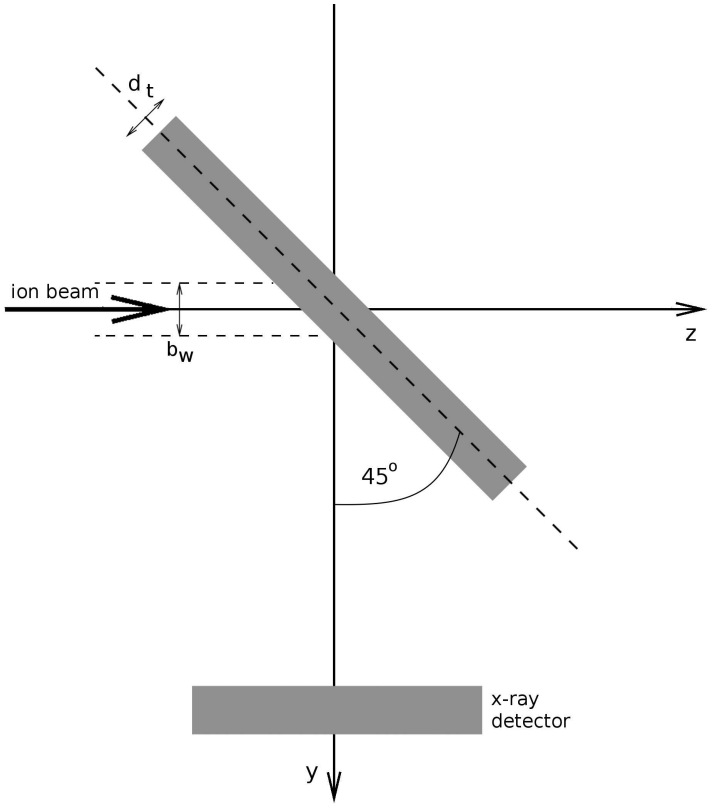


Figure 7.1: Geometry of the experimental setup implemented in the Monte Carlo simulation, b_w – the beam diameter, d_t – target thickness in mm. The x-axis is perpendicular to the picture plane.

It was assumed that the beam propagates in the z direction, while the center of the x-ray detector is positioned at $x = 0$ and at positive values of y (compare Figs. 4.6 and 7.1). The primary method for determination of the collision coordinates (x, y, z) within the target (see Chapter 3 of [Swi 00]) was replaced by:

$$\begin{cases} x = b_w(Rand - 0.5), \\ y = b_w(Rand - 0.5), \\ z = d_t(Rand - 0.5) + y \tan\left(\frac{\pi}{4}\right), \end{cases} \tag{7.1}$$

where b_w is the beam diameter and d_t is the target thickness, both given in mm. $Rand \in [0; 1]$ is provided by a random number generator. The beam transverse cross section was assumed to be a circle, thus the (x, y) coordinates were limited by:

$$x^2 + y^2 \leq \left(\frac{b_w}{2}\right)^2. \tag{7.2}$$

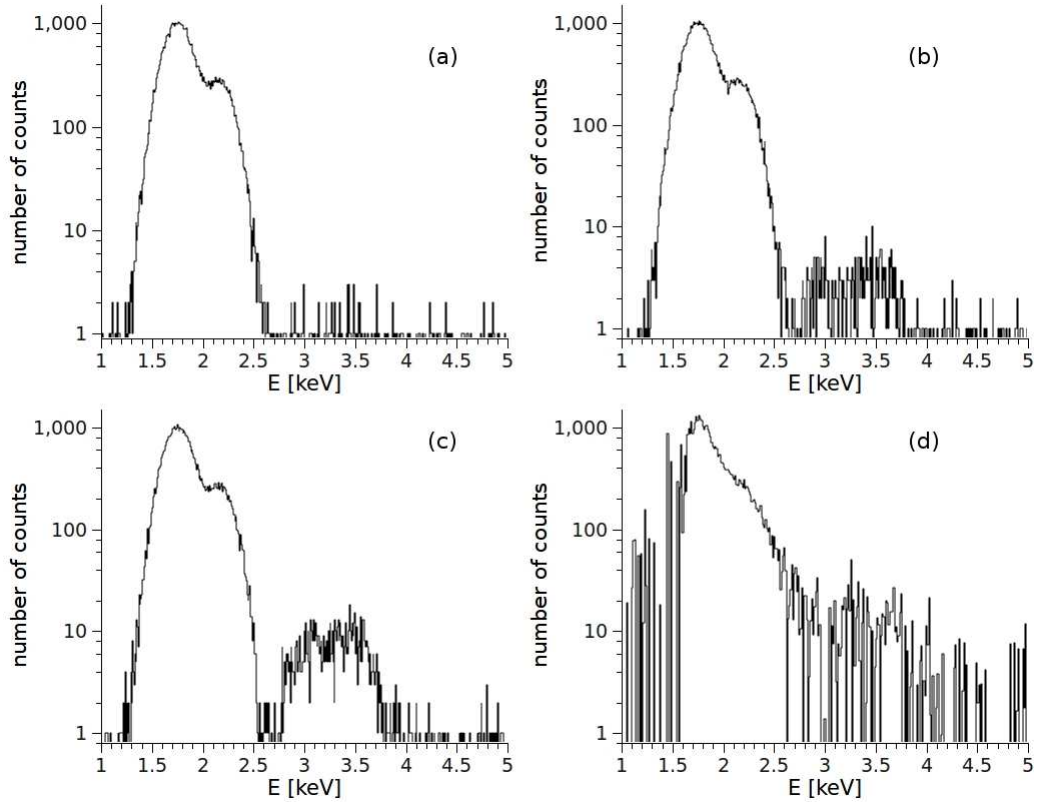


Figure 7.2: Monte Carlo simulated x-ray spectra: (a) no RDEC included, (b) the RDEC cross section as given by Nefiodov, (c) $\sigma^{1s^2}_{RDEC} = 3$ b and $\sigma^{1s^12s^1}_{RDEC} = 2.1$ b – cross sections values for which MC simulation gives the results closest to the experimental data. (d) Experimentally obtained singles spectrum.

The REC and DREC processes were implemented with the cross sections of 512 b and 48 b, respectively, as given in Table 5.3. As shown in the previous chapter, the RDEC structure observed in x-ray spectra consisted mainly of two lines. In order to simulate this double structure of the RDEC line (i.e. capture to the ground ($1s^2$) and excited ($1s^12s^1$) state), the input data included two kinds of the RDEC processes: capture to the ground state with the cross section of $\sigma^{1s^2}_{RDEC}$ and capture to the excited state with cross section of $\sigma^{1s^12s^1}_{RDEC} = 0.7\sigma^{1s^2}_{RDEC}$ estimated according to [Nef 05]. As the photon angular distributions for neither RDEC nor DREC is known, they were assumed to be the same as for the REC photons, that is $\sim \sin^2\theta$. Additionally, the DREC photons were considered to be emitted independently of each other, as discussed in Section 5.4.

During the first step of the simulation, RDEC was not included in the input data. The obtained spectrum is shown in Fig. 7.2 (a). It can be noticed that only a few counts showed

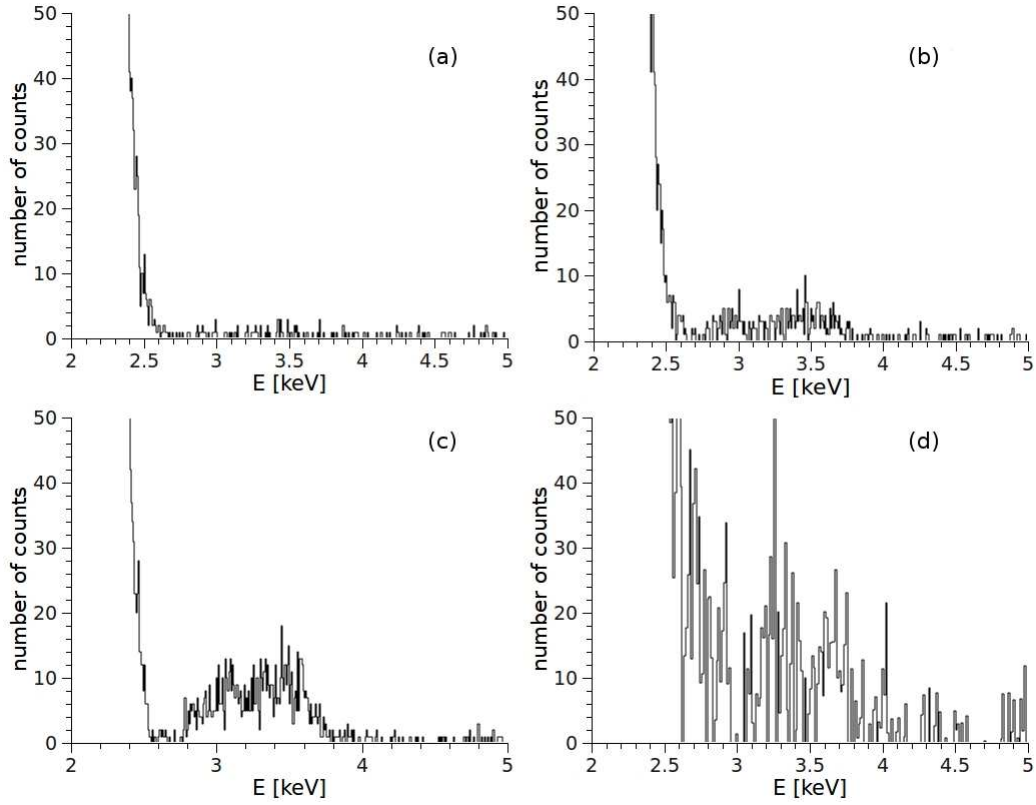


Figure 7.3: The RDEC range of the x-ray spectra. Results of simulations: (a) no RDEC included, (b) the RDEC cross section as given by Nefiodov, (c) $\sigma^{1s^2}_{RDEC} = 3$ b and $\sigma^{1s^12s^1}_{RDEC} = 2.1$ b – cross sections values for which MC simulation gives the results closest to the experimental data. (d) Experimentally obtained single spectrum

up in the RDEC energy range. These counts are due to simultaneous detection of both the DREC photons. Comparison with the results in Fig. 7.2 (d) shows clearly that DREC itself cannot explain the experimental results. Moreover, the result of the simulation shows that the contribution of a pile-up effect of the DREC photons is not significant as mentioned in Section 5.4.

The second step of the simulations was implementation of the RDEC process with the cross sections $\sigma^{1s^2}_{RDEC} = 0.15$ b [Nef 09] and $\sigma^{1s^12s^1}_{RDEC} = 0.7\sigma^{1s^2}_{RDEC} = 0.105$ b [Nef 05] for the capture to the ground and the excited state, respectively. Again, the results showed that this was not sufficient to explain the experimental data (compare Figs 7.2 (b) and (d)).

During the third step of the simulation the RDEC cross section was increased until the resulting spectrum was comparable with the experimental one (Fig. 7.2 (d)). The best results, shown in Fig. 7.2 (c), were obtained for $\sigma^{1s^2}_{RDEC} = 3$ b and $\sigma^{1s^12s^1}_{RDEC} = 0.7\sigma^{1s^2}_{RDEC} = 2.1$ b.

Table 7.1: Ratios of the numbers of counts in the RDEC and REC regions obtained during Monte Carlo simulations compared with the experimental value.

	RDEC cross section [b]	Number of counts		RDEC/REC ratio
	$\sigma^{1s^2}_{RDEC} + \sigma^{1s^1 2s^1}_{RDEC}$	REC range	RDEC range	
simulation	0	40100(180)	71(8)	0.0018(2)
	0.15 + 0.105	39900(180)	225(8)	0.0056(5)
	3 + 2.1	39700(180)	449(20)	0.0113(3)
experiment	3.2 + 2.3	39800(200)	357(28)	0.0092(6)

However, it can be noticed that the RDEC structure within the experimentally obtained spectrum (Fig. 7.2 (d)) is placed on the REC tail, which seems to be much broader than the simulated one. This may be due to the fact that for the simulation the Compton profile of diamond was used as given by Reed [Ree 72], which might differ from the one for the amorphous carbon foil that was used during the experiment. However, the main purpose of the simulation was to investigate the ratio of the numbers of counts related to the RDEC and REC processes, thus the Compton profile here is of a minor importance.

In Fig. 7.3 only the RDEC range of all the spectra was shown on the linear scale, for better visualization of the double structure of the RDEC line. As a test of the result of the simulations, the ratio of the numbers of counts in the RDEC and REC range was calculated. The obtained values are shown in Table 7.1. It can be seen that the results of the third step of the simulation are in the best agreement with the experimental data. This again shows that the cross section value calculated by Nefiodov, even when capture to the excited state is included, is insufficient to explain the experimental results.

Chapter 8

Conclusions

In this dissertation an experiment dedicated to the radiative double electron capture process (RDEC) was presented. The experiment was carried out at Western Michigan University using the 6 MV tandem Van de Graaff accelerator. The choice of the collision system, O^{8+} + C at 38 MeV, was based on the recent theoretical calculations of the RDEC cross section [Mik 04a, Mik 04b, Nef 05], which pointed to mid-Z ions and low collision energy as the best systems for observation of RDEC. The theoretical approach also suggested an enhancement of the RDEC cross section in such systems due to capture of electrons from the target valence band. Moreover, it was pointed out that the capture to the excited state of the projectile may be a significant contribution to the process.

The results allowed for the first experimental verification of RDEC and provided a test of the main theoretical predictions [Mik 04a, Mik 04b, Nef 05]. The obtained x-ray spectra revealed a complex structure of the RDEC line. However, the capture from the target valence band, which, according to the theory, was supposed to significantly contribute to the RDEC process, was not confirmed. The observed structure allowed for identification of capture to the projectile ground ($1s^2$) and excited ($1s^12s^2$) states. The ratio of the counts which could be associated with these two processes gave a ratio of the RDEC cross sections for the capture to the excited and the ground states $\sigma^{1s^12s^2}_{RDEC}/\sigma^{1s^2}_{RDEC} = 0.500(68)$, which is close, considering the data statistics, to the theoretical value of 0.7.

The latter value, together with the observed ratio of the numbers of counts in the RDEC and REC range of the x-ray spectra, $N_{RDEC}/N_{REC} = 0.0092(6)$, allowed for estimation of the RDEC cross sections:

- $\sigma^{1s^2}_{RDEC} = 3.2(1.9)$ b for the capture to the ground state,

Table 8.1: Summary of the results of the theoretical calculations and the experiments dedicated to the RDEC process.

Z	E [MeV/u]	ξ	Z_t	$\sigma^{1s^2}_{RDEC}$ [mb]		
				Ref. [Mik 04a]	Ref. [Yak 97]	experiment
18	11.4	0.840	6	3.2	1.85	$\leq$5.2 [War 95]
92	297	0.841	18	$2.5{\cdot}10^{-2}$	5000	$\leq$10 [Bed 03]
8	2.375	0.820	6	$1.5{\cdot}10^{2}$ $^{(a)}$	$1.4{\cdot}10^{2}$ $^{(b)}$	$3.2(1.9){\cdot}10^{3}$ $^{(c)}$

$^{(a)}$ provided by Nefiodov [Nef 09]

$^{(b)}$ estimated from the $R_{Yakh} = \sigma^{1s^2}_{RDEC}/\sigma_{REC}$ ratio

$^{(c)}$ this experiment

- $\sigma^{1s^1 2s^1}_{RDEC} = 2.3(1.3)$ b for the capture to the excited state.

The main results of the experiment have already been published [Sim 10]. The obtained value of the cross section is a factor of about 25 greater than the theoretical value provided by Nefiodov [Nef 09]. Consequently, the ratio $R = \sigma^{1s^2}_{RDEC}/\sigma_{REC} = 0.0074(37)$ is also significantly greater than estimated from the theory, as shown in Table 8.1.

The results of the so far conducted experiments dedicated to the RDEC process are given in Table 8.1 . The discrepancies between the theories and experiments, as well as the differences between various theoretical approaches, show that further investigation of the RDEC process is necessary. A similar experiment chould be performed, with the same experimental setup available at WMU, but with an additional absorbing material in front of the x-ray detector. This will exclude all the pile-up effects and contributions of the DREC process, which formed a crucial problem of the background analysis in the presented experiment. Moreover, the angular distribution and correlations of the DREC photons should be measured as DREC interferes with other radiative capture processes.

As the role of the capture from the valence band of the solid target was not verified, application of a gas jet target with a light gas (He) would be useful, due to a significant reduction of background and a much smaller probability of multiple collisions. Additionally, a system with a greater difference between projectile and target atomic number (for example Ca^{20+}, Ar^{18+} or Xe^{54+} on He) would allow for better separation of photons originating from the capture to the ground and excited state of the projectile. All these conditions can be satisfied during an experiment on the ESR gas jet target at GSI.

Appendix A

Statistical analysis of the observed signal

In order to check if the observed structure within a given region of the spectrum is a result of a physical process or just a statistical fluctuation, a method suggested in [Ead 89] was applied. Here, a brief description of the approach is presented.

Alternatively, one can calculate the probability of observation of a statistical fluctuation within the range of interest. This method assumes that the background distribution is known.

A null hypothesis can be defined as:

H_0: there is no physical effect within the AB range.

It is assumed that the background shape can be described by a function $b(\mathbf{x}, \mathbf{\Theta})$, which depends on the observed variable $\mathbf{x}$ and unknown parameters $\mathbf{\Theta}$. In this case the number of the background counts in the AB region (Fig. A.1) is given by:

$$\hat{b}_{AB} = \int_A^B b(\mathbf{x}, \hat{\mathbf{\Theta}}) d\mathbf{x}. \tag{A.1}$$

As $\hat{b}_{AB}$ is a function of estimators $\hat{\mathbf{\Theta}}$, the variance can be obtained by a substitution of variables:

$$\hat{\sigma}^2_{AB} = \mathbf{D}^T \tilde{V} \mathbf{D}, \tag{A.2}$$

where $\mathbf{D}$ denotes a vector of derivatives:

$$D_i = \frac{\partial \hat{b}_{AB}}{\partial \Theta_i}\Big|_{\hat{\mathbf{\Theta}}_i} = \int_A^B \frac{\partial}{\partial \Theta_i} b(\mathbf{x}, \hat{\mathbf{\Theta}}) dx \tag{A.3}$$

If N_{AB} denotes the number of events in the AB range, the optimal test statistic, which checks if N_{AB} significantly differs from $\hat{b}_{AB}$, is:

$$T = \frac{(N_{AB} - \hat{b}_{AB})^2}{V(N_{AB} - \hat{b}_{AB})}, \tag{A.4}$$

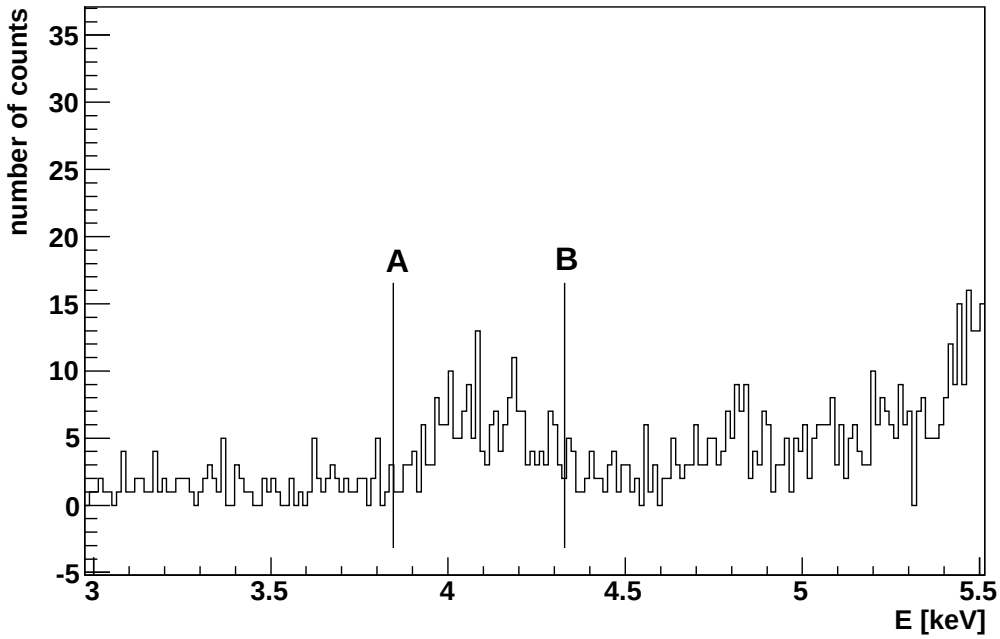


Figure A.1: Example of an experimentally obtained spectrum with a structure within the AB range.

where $V(N_{AB} - \hat{b}_{AB})$ is a variance. If the H_0 hypothesis is true, then:

$$E(N_{AB}) = b_{AB} \tag{A.5}$$

$$V(N_{AB}) = b_{AB} \tag{A.6}$$

where $E(N_{AB})$ is the estimator of the number of counts in the AB region and the estimator of b_{AB} is $\hat{b}_{AB}$. Thus:

$$V(N_{AB} - \hat{b}_{AB}) \approx \hat{b}_{AB} + \hat{\sigma}^2_{AB} - 2cov(N_{AB}, \hat{b}_{AB}). \tag{A.7}$$

As during the estimation of Θ parameters the AB range was excluded, N_{AB} and $\hat{b}_{AB}$ are uncorrelated:

$$V(N_{AB} - \hat{b}_{AB}) \approx \hat{b}_{AB} + \hat{\sigma}^2_{AB} \tag{A.8}$$

and

$$T = \frac{(N_{AB} - \hat{b}_{AB})^2}{\sigma^2_{AB} + \hat{b}_{AB}}. \tag{A.9}$$

If the number of counts N_{AB} is large, it has a normal distribution around $\hat{b}_{AB}$ and the statistic T behaves as a χ^2 distribution for $DoF = 1$ (degrees of freedom).

Table A.1: Quantiles of the χ^2 distribution for $DoF = 1$ [Kam].

α	0.005	0.010	0.020	0.025	0.050	0.100	0.250	0.300	0.500
χ^2	4.0E-5	0.0002	0.0006	0.0010	0.0039	0.0642	0.1015	0.1485	0.4549
α	0.700	0.750	0.800	0.900	0.950	0.975	0.990	0.995	0.999
χ^2	1.0742	1.3233	1.6424	2.7055	3.8415	5.4119	6.6349	7.8794	10.8270

For the obtained value of the statistical variable T the value of α_T can be estimated based on Table A.1. If $(1 - \alpha_T) > \alpha$, where α is the probability of the type one error, the hypothesis can be accepted. The deviation is small enough for chance alone to account for it. If $(1 - \alpha_T) < \alpha$, the hypothesis should be rejected, as there may be some factor other than chance operating for the deviation to be so great.

If, based on statistics A.9, H_0 was rejected, estimation of the signal $s = N_{AB} - \hat{b}_{AB}$ can still be used, but with a different estimator variance. The problem one is about to solve is now a test of hypothesis H_1 against hypothesis H_0.

H_1: there is a physical signal s and background $\hat{b}_{AB}$ in the AB range.

In this case the variance will be given by:

$$V(N_{AB} - \hat{b}_{AB}) \approx N_{AB} + \hat{\sigma}^2_{AB}, \tag{A.10}$$

where, for the same reason as in Eq. A.8, covariance is not included. The risk of making a type two error is equal to:

$$\beta = P(d \leq \lambda_\alpha | H_1), \tag{A.11}$$

where $d = \sqrt{T}$ and λ_α is defined by $\Phi(\lambda_\alpha) = \alpha$, Φ being a cumulative normal distribution function, given by:

$$\Phi(x) = \frac{1}{\sqrt{2\pi}} \int_{-\infty}^{x} e^{-t^2/2} dt. \tag{A.12}$$

For the H_1 hypothesis the mean value and variance are given by:

$$E(N_{AB}) = V(N_{AB}) = b_{AB} + s, \tag{A.13}$$

while d has a normal distribution $\mathbf{N}(\mu, \sigma^2)$, where:

$$\mu = \frac{s}{\sqrt{\hat{b}_{AB} + \hat{\sigma}^2_{AB}}}, \tag{A.14}$$

$$\hat{\sigma}^2 = \frac{\hat{b}_{AB} + s + \hat{\sigma}^2_{AB}}{\hat{b}_{AB} + \hat{\sigma}^2_{AB}}. \tag{A.15}$$

Thus, finally:

$$\beta = \Phi \left[\frac{\lambda_\alpha \sqrt{\hat{b}_{AB} + \hat{\sigma}^2_{AB}} - s}{\sqrt{\hat{b}_{AB} + s + \hat{\sigma}^2_{AB}}} \right]. \tag{A.16}$$

List of References

[ACF 09] ACF-Metals. "Product specification". http://techexpo.com/WWW/acf-metals/page1.html, January 2009.

[Amu 75] M. Y. Amusia, E. G. Drukarev, V. G. Gorshkov, and M. P. Kazachkov. *J. Phys. B*, Vol. 8, p. 1248, 1975.

[Bed 03] G. Bednarz, D. Sierpowski, T. Stoehlker, A. Warczak, H. B. b, F. Bosch, A. Braeuning-Demian, H. Braeuning, X. Cai, A. Gumberidze, S. Hagmann, C. Kozhuharov, D. Liesen, X. Ma, P. Mokler, A. Muthig, Z. Stachura, and S. Toleikis. *Nucl. Instr. Meth. B*, Vol. 205, p. 573, 2003.

[Bed 98] G. Bednarz, A. Warczak, H. Tawara, T. Azuma, K. Komaki, and E. Takada. *Eur. Phys. J. D*, Vol. 4, p. 271, 1998.

[Ber 93] N. Berrah, F. Heiser, R. Wehlitz, J. Levin, S. B. Witfield, J. Viefhaus, I. A. Sellin, and U. Becker. *Phys. Rev. A*, Vol. 48, p. R1733, 1993.

[Bey 03] H. F. Beyer and V. P. Shevelko. *Introduction to the Physics of Highly Charged Ions.* Insitute of Physics Publishing, Boston, Philadelphia, 2003.

[Big 75] F. Biggs, L. B. Mendelsohn, and J. B. Mann. *Atomic Data and Nuclear Data Tables*, Vol. 16, p. 201, 1975.

[Bom 89] S. Boman, E. M. Bernstein, and J. A. Tanis. *Phys. Rev. A*, Vol. 39, p. 4423, 1989.

[Car 77] S. L. Carter and H. P. Kelly. *Phys. Rev. a*, Vol. 16, p. 1525, 1977.

[Car 81] S. L. Carter and H. P. Kelly. *Phys. Rev. A*, Vol. 24, p. 170, 1981.

[Chu 81] T. C. Chu, K. Ishii, A. Yamadera, M. Sebata, and S. Morita. *Phys. Rev. A*, Vol. 24, p. 1720, 1981.

[Dal 94] A. Dalgarno and H. R. Sadeghpour. *Comments At. Mol. Phys.*, Vol. 30, p. 143, 1994.

[Dru 07] E. G. Drukarev, A. I. Mikhailov, A. I. Mikhailov, and W. Scheid. *Phys Rev. A*, Vol. 76, p. 1062701, 2007.

[Ead 89] W. T. Eadie, D. Drijard, F. E. James, M. Roos, and B. Sadoulet. *Metody statystyczne w fizyce doświadczalnej.* PWN, 1989.

[Edw 93] D. A. Edwards and M. J. Syphers. *An Introduction to the Physics of High Energy Accelerators.* John Wiley and Sons, Inc., 1993.

[Eic 07] J. Eichler and T. Stoehlker. *Phys. Rep.*, Vol. 439, p. 1, 2007.

[Eic 95a] J. Eichler, A. Ichihara, and T. Shirai. *Phys. Rev. A*, Vol. 51, p. 3027, 1995.

[Eic 95b] J. Eichler and W. E. Meyerhof. *Relativistic Atomic Collisions.* Academic, San Diego, 1995.

[Ein 05] A. Einstein. *Ann. Phys.*, Vol. 17, p. 132, 1905.

[Fan 59] U. Fano, K. W. McVoy, and J. R. Albers. *Phys. Rev.*, Vol. 116, p. 1147, 1959.

[Fol 75] F. Folkmann, K. O. Groeneveld, R. Mann, G. Nolte, S. Schumann, and R. Spohr. *Z. Physik A*, Vol. 275, p. 229, 1975.

[Fol 84] F. Folkmann, K. Cramon, and N. Hertel. *Nucl. Instr. Meth.*, Vol. 3, p. 11, 1984.

[Gra 31] R. J. V. de Graaff. *Phys. Rev.*, Vol. 38, p. 1919, 1931.

[Gra 47] R. J. V. de Graaff, J. G. Trump, and M. W. Buechner. *Rep. Prog. Phys.*, Vol. 11, p. 1, 1947.

[Gra 84] W. G. Graham, K. H. Berkner, R. V. Pyle, A. S. Schlachter, J. W. Stearns, and J. A. Tanis. *Phys. Rev. A*, Vol. 30, p. 722, 1984.

[Gra 85] W. G. Graham, K. H. Berkner, E. M. Bernstein, M. Clark, R. H. McFarland, T. J. Morgan, A. S. Schlachter, J. W. Stearns, M. P. Stockli, and J. A. Tanis. *J. Phys. B*, Vol. 18, p. 2503, 1985.

[Gri 01] D. J. Griffiths. *Podstawy elektrodynamiki.* PWN Warszawa, 2001.

[Her 87] H. Hertz. *Ann. Phys.*, Vol. 267, p. 983, 1887.

[Hin 87] K. Hino and T. Watanabe. *Phys. Rev. A*, Vol. 36, p. 581, 1987.

[Hin 97] F. Hinterberger. *Physik der Teilchenbeschleuniger und Ionenoptik*. Springer, 1997.

[Hip 87] R. Hippler, S. Datz, P. D. Miller, P. L. Pepmiller, and P. F. Dittner. *Phys. Rev. A*, Vol. 35, p. 585, 1987.

[Ich 94] A. Ichihara, T. Shirai, and J. Eichler. *Phys. Rev. A*, Vol. 49, p. 1875, 1994.

[Ich 96] A. Ichihara, T. Shirai, and J. Eichler. *Phys. Rev. A*, Vol. 54, p. 4954, 1996.

[Ish 06] K. Ishii. *Rad. Phys. Chem.*, Vol. 75, p. 1135, 2006.

[Ish 87] K. Ishii and S. Morita. *Nucl. Instr. Meth. B*, Vol. 22, p. 68, 1987.

[Jak 06] D. H. Jakubassa-Amundsen. *Rad. Phys. Chem.*, Vol. 75, p. 1319, 2006.

[Kam] B. Kamys. http://users.uj.edu.pl/ ufkamys/BK/kwantyle.pdf.

[Kan 95] T. Kandler, T. Stoehlker, P. H. Mokler, C. Kozhuharov, H. Geissel, C. Scheidenberg, P. Rymuza, Z. Stachura, A. Warczak, R. W. Dunford, J. Eichler, and T. Schirai. *Z. Phys. D*, Vol. 35, p. 15, 1995.

[Kay] A. Kayani. http://www.tesla.physics.wmich.edu/acceleratorlab.

[Kie 73] P. Kienle, M. Kleber, B. Povh, R. M. Diamond, F. S. Stephens, E. Grosse, M. R. Maier, and D. Proetel. *Phys. Rev. Lett.*, Vol. 31, p. 1099, 1973.

[Lab 87] P. Lablanquie, J. H. D. Eland, I. Nenner, P. Morin, J. Delwiche, and M.-J. Hubin-Franskin. *Phys. Rev. Lett.*, Vol. 58, p. 992, 1987.

[Lan 79] L. D. Landau and E. M. Lifszyc. *Mechanika kwantowa. Teoria nierelatywistyczna.* PWN Warszawa, 1979.

[Lip 00] R. Lipton. http://www-ppd.fnal.gov/eppoffice-w/Academic_Lectures/new_sil_lect.pdf, 2000.

[Lud 98] T. Ludziejewski, T. Stoehlker, S. Keller, H. Beyer, F. Bosch, O. Brinzanescu, R. W. Dunford, B. Franzke, C. Kozhoharov, D. Liesen, A. E. Livingstone, G. Menzel,

J. Meier, P. H. Mokler, H. Reich, P. Rymuza, Z. Stachura, M. Steck, L. Stenner, P. Swiat, and A. Warczak. *J. Phys. B*, Vol. 31, p. 2601, 1998.

[Mey 85] W. E. Meyerhof, R. Anholt, J. Eichler, H. Gould, C. Munger, J. Alonzo, P. Thieberger, and H. E. Wegner. *Phys. Rev. A*, Vol. 32, p. 3291, 1985.

[Mik 04a] A. I. Mikhailov, I. A. Mikhailov, A. Nefiodov, G. Plunien, and G. Soff. *Phys. Lett. A*, Vol. 328, p. 350, 2004.

[Mik 04b] A. I. Mikhailov, I. A. Mikhailov, A. N. M. A. Nefiodov, G. Plunien, and G. Soff. *Phys. Rev. A*, Vol. 69, p. 032703, 2004.

[Mir 89] J. Miraglia. *Phys. Rev. A*, Vol. 39, p. 2908, 1989.

[Mok 78] P. H. Mokler and F. Folkman. "X-ray Production in Heavy Ion-Atom Collisions". In: I. Sellin, Ed., *Structure and Collisions of Ions and Atoms*, Springer-Verlag, 1978.

[Mok 95] P. H. Mokler, T. Stoehlker, R. W. Dunford, A. Gallus, T. Kandler, G. Mentzel, H. T. Prinz, Z. Stachura, P. Świat, and A. Warczak. *Z. Phys. D*, Vol. 35, p. 77, 1995.

[Nef 05] A. Nefiodov, A. I. Mikhailov, and G. Plunien. *Phys Lett. A*, Vol. 346, p. 158, 2005.

[Nef 09] A. Nefiodov. *private communication*, 2009.

[Ols 78] R. E. Olson, K. H. Berkner, W. G. Graham, R. V. Pyle, A. S. Schlachter, and J. W. Stearns. *Phys. Rev. Lett.*, Vol. 41, p. 163, 1978.

[ORTa] ORTEC. http://www.ortec-online.com/detectors/photon/b2_4_6.htm.

[ORTb] ORTEC. http://www.ortec-online.com/detectors/review_physics/pulse.htm.

[Ree 72] W. A. Reed and P. Eisenberger. *Phys. Rev. B*, Vol. 6, p. 4596, 1972.

[Roe 96] W. C. Roentgen. *Nature*, Vol. 53, p. 274, 1896.

[Roe 98] W. C. Roentgen. *Ann. Phys.*, Vol. 300, p. 12, 1898.

[Sai 92] N. Saito and I. H. Suzuki. *Phys. Scr.*, Vol. 45, p. 253, 1992.

[Sch 72] H. W. Schnopper, H. D. Betz, J. P. Delvaille, K. Kalata, A. R. Sohval, K. W. Jones, and H. E. Wegner. *Phys. Rev. Lett.*, Vol. 29, p. 898, 1972.

[Sch 74] H. W. Schnopper, J. P. Delvaille, K. Kalata, A. R. Sohval, M. Abdulwahab, K. W. Jones, and H. E. Wegner. *Phys. Lett.*, Vol. 47 A, p. 61, 1974.

[Sch 83] A. S. Schlachter, J. W. Stearns, W. G. Graham, K. H. Berkner, R. V. Pyle, and J. A. Tanis. *Phys. Rev. A*, Vol. 27, p. 3372, 1983.

[Sch 93] K.-H. Schartner, G. Mentzel, B. Magel, B. Moebus, A. Ehresmann, F. Vollweiler, and H. Schmoranzer. *J. Phys. B*, Vol. 26, p. L445, 1993.

[Shi 92] K. Shima, N. Kuno, M. Yamanouchi, and H. Tawara. *At. Data and Nucl. Data Tables*, Vol. 51, p. 173, 1992.

[Sim 10] A. Simon, A. Warczak, T. ElKafrawy, and J. A. Tanis. *Phys. Rev. Lett*, Vol. 104, p. 123001, 2010.

[Smi 89] Z. Smit, M. Kregar, and D. Glavic-Cindro. *Phys. Rev. A*, Vol. 40, p. 6303, 1989.

[Soh 76] A. R. Sohval, J. P. Delvaille, K. Kalata, K. Kirby-Docken, and H. W. Schnopper. *J. Phys. B*, Vol. 9, p. L25, 1976.

[Spi 79] E. Spindler, H. D. Betz, and F. Bell. *Phys. Rev. Lett.*, Vol. 42, p. 832, 1979.

[Sto 30] M. Stobbe. *Ann. Phys.*, Vol. 7, p. 661, 1930.

[Sto 92] T. Stoehlker, C. Kozhuharov, A. E. Livingstone, P. H. Mokler, Z. Stachura, and A. Warczak. *Z. Phys. D*, Vol. 23, p. 121, 1992.

[Sto 94] T. Stoehlker, H. Giessel, H. Irnich, T. Kandler, C. Kozhuharov, P. Mokler, G. Muenzenberg, F. Nickel, C. Scheidenberger, T. Suzuki, M. Kucharski, A. Warczak, P. Rymuza, Z. Stachura, A. Kriessbach, and T. Shirai. *Phys. Rev. Lett.*, Vol. 73, p. 3520, 1994.

[Sto 95a] T. Stoehlker, F. Bosch, H. Geissel, T. Kandler, C. Kozhuharov, P. H. Mokler, R. Moshammer, P. Rymuza, C. Schneidenberger, Z. Stachura, A. Warczak, J. Eichler, A. Ichihara, and T. Schirai. *Nucl. Instr. Meth. B*, Vol. 98, p. 235, 1995.

[Sto 95b] T. Stoehlker, C. Kozhuharov, P. H. Mokler, A. Warczak, F. Bosch, H. Geissel, R. Moshammer, C. Scheidenberger, J. Eichler, A. Ichihara, T. Shirai, Z. Stachura, and P. Rymuza. *Phys Rev. A*, Vol. 51, p. 2098, 1995.

[Sto 97a] T. Stoehlker, F. Bosch, A. Gallus, C. Kozhuharov, G. Menzel, P. H. Mokler, H. T. Prinz, J. Eichler, A. Ichihara, T. Shirai, R. W. Dunford, T. Ludziejewski, P. Rymuza, Z. Stachura, P. Świat, and A. Warczak. *Phys. Rev. Lett.*, Vol. 79, p. 3270, 1997.

[Sto 97b] T. Stoehlker, P. H. Mokler, C. Kozhuharov, and A. Warczak. *Comm. At. Mol. Phys.*, Vol. 33, p. 271, 1997.

[Sto 98] T. Stoehlker, T. Ludziejewski, H. Reich, F. Bosch, R. W. Dunford, J. Eichler, B. Franzke, C. Kozhuharov, G. Menzel, P. H. Mokler, F. Nolden, P. Rymuza, Z. Stachura, M. Steck, P. Świat, A. Warczak, and T. Winkler. *Phys. Rev. A*, Vol. 58, p. 2043, 1998.

[Swi 00] P. Swiat. *Procesy atomowe w zderzeniach ciężkich jonów z atomami przy prędkościach relatywistycznych.* PhD thesis, Jagiellonian University, 2000.

[Swi 99] P. Swiat, A. Warczak, T. Stoehlker, F. Bosch, C. Kozhuharov, P. H. Mokler, H. Reich, R. W. Dunford, P. Rymuza, T. Ludziejewski, and Z. Stachura. *Phys. Scr T*, Vol. 80, p. 326, 1999.

[Tan 81] J. A. Tanis, S. M. Shafroth, J. E. Willis, and J. R. Mowat. *Phys. Rev. A*, Vol. 23, p. 366, 1981.

[Tan 87] J. A. Tanis, M. W. Clark, K. H. Berkner, E. M. Bernstein, W. G. Graham, R. J. McDonald, R. H. McFarland, J. R. Mowat, D. W. Mueller, A. S. Schlachter, J. W. Stearns, and M. P. Stockli. *J. de Phys.*, Vol. C9, p. 207, 1987.

[Tan 91] J. A. Tanis, E. M. Bernstein, M. W. Clark, S. M. Ferguson, and R. N. Prince. *Phys. Rev. A*, Vol. 43, p. 4723, 1991.

[Tho 01] A. C. Thompson and D. Vaughan, Eds. *X-ray Data Booklet.* Lawrence Berkeley National Laboratory, January 2001.

[Tiw 82] S. N. Tiwary. *J. Phys. B*, Vol. 15, p. L323, 1982.

[War 95] A. Warczak, M. Kucharski, Z. Stachura, H. Giessel, H. Irnich, T. Kandler, C. Kozhuharov, P. Mokler, G. Muenzenberg, F. Nickel, C. Scheidenberger, T. Stoehlker, T. Suzuki, and P. Rymuza. *Nucl. Inst. Meth. B*, Vol. 98, p. 303, 1995.

[Wed 99] H. Wedermann. *Particle Accelerator Physics I. Basic Principles and Linear Beam Dynamics*. Springer, 1999.

[Yak 96] V. L. Yakhontov and M. Y. Amusia. *Phys. Lett. A*, Vol. 221, p. 328, 1996.

[Yak 97] V. L. Yakhontov and M. Y. Amusia. *Phys. Rev. A*, Vol. 55, p. 1952, 1997.